Mineralogy and chemistry of San Carlos high-alkali basalts: Analyses of alteration with application for Mars exploration⚏

BRYNÉ A. HADNOTT[1,2,*], BETHANY L. EHLMANN[2,3], AND BRADLEY L. JOLLIFF[1]

[1]Department of Earth and Planetary Sciences, Washington University in St. Louis, St. Louis, Missouri 63105, U.S.A.
[2]Division of Geological and Planetary Sciences, California Institute of Technology, Pasadena, California 91125, U.S.A.
[3]Jet Propulsion Laboratory, California Institute of Technology, Pasadena, California 91109, U.S.A.

ABSTRACT

The discovery of Fe, Mg, and Al phyllosilicates on Mars using visible and short-wave infrared (VSWIR) spectroscopy from orbit indicates aqueous alteration of basaltic rocks. Analyses at Gusev Crater by the Spirit rover and Gale Crater by the Curiosity rover have discovered alkaline basaltic rocks. In this work, multiple methods—VSWIR spectroscopy, X-ray diffraction (XRD), and chemical analyses—were used to study a suite of alkaline basalts from San Carlos, Arizona, which have been altered by water in an oxidative, semi-arid environment. As an analog for the weathering of alkaline basaltic rocks on Mars, a suite of rocks visually identified to have different degrees of alteration were characterized to understand the spectral, mineralogical, and chemical trends in alteration as sensed by multiple techniques. Samples with strong 1.9 μm H_2O-related absorptions in VSWIR commonly exhibited absorption bands at 1.4, 2.2, and/or 2.3 μm, indicating the presence of clay minerals or silica as well as features at 0.5–0.9 μm indicative of ferric iron oxides. Primary mineralogy for all samples, as determined by point analyses with the microprobe and XRD, consisted of olivine, plagioclase, nepheline, augite, and titanomagnetite. Compositional imaging and spot analyses with the microprobe revealed distinct alteration textures and phases, suggesting weathering pathways involving the oxidation of iron in olivine and primary Fe^{2+} oxides to form Fe^{3+} oxides as well as the formation of aluminum phyllosilicates and magnesium phyllosilicates from feldspars and olivines, respectively, while pyroxene remained relatively unaltered. Bivariate plots of major oxides both from bulk-chemical analysis and microprobe measurements also revealed trends in alkali and silica depletion and calcium enrichment, but there was little chemical fractionation in most of the major oxides. The strength of the 1.9 μm H_2O absorption, loss on ignition, and depletion in silica and sodium, correlated with increasing alteration. The data sets provide an analog for understanding possible weathering pathways in martian alkaline basalts and thresholds for the detection of aqueous alteration in multiple data sets.

Keywords: VSWIR spectroscopy, Mars analogs, XRD, geochemistry, alkali basalts, San Carlos

INTRODUCTION

Orbiting visible and near-infrared spectrometers, and data from landed missions, have revealed a diverse array of aqueous environments preserved in the rock record from ancient Mars. The vast majority of the surface of Mars is basaltic in composition (e.g., Rogers and Christensen et al. 2007), but sulfates, chlorides, carbonates, and hydrated silicates have been detected by orbiting spectrometers and confirmed by rover data (e.g., Bibring et al. 2006; Mustard et al. 2008; Ehlmann and Edwards 2014; Grotzinger et al. 2015). Currently, the Mars Science Laboratory Curiosity rover is exploring Gale Crater, a site that hosts a diverse array of lithologies, including suites of rocks that are more alkali-rich than other martian basalts, as revealed by analyses with the ChemCam laser-induced breakdown spectroscopy instrument (LIBS) (Wiens

et al. 2012, 2013; Maurice et al. 2012; Cousin et al. 2015; Sautter et al. 2015; Vasavada et al. 2014) and the alpha particle X-ray spectrometer (APXS) (Gellert et al. 2013). Jake Matijevic, the first target analyzed by both ChemCam and APXS, is interpreted to be a fine-grained igneous rock with an alkaline composition similar to nepheline-normative mugearites (Stolper et al. 2013; Blaney et al. 2014). Three other rock targets, and multiple other rocks and clasts measured remotely by ChemCam, were found to have alkaline basalt compositions and to plot in the basanite field on a total alkali silica (TAS) diagram (Fig. 1), suggesting alkali-rich igneous protoliths as source material for sedimentary rocks and a greater diversity of martian igneous compositions (Schmidt et al. 2014; Meslin et al. 2013; Sautter et al. 2014). Similarly, alkaline suites of rocks have also been measured in the Columbia Hills, Gusev crater by the Spirit rover (McSween et al. 2006). Collectively, these data suggest unique types of martian volcanism and/or aqueous alteration to explain their geochemistry (McSween et al. 2006; Schmidt et al. 2014; Udry et al. 2014).

To date, most spectral libraries and analyses of aqueous alteration of igneous protoliths as Mars analogs have focused
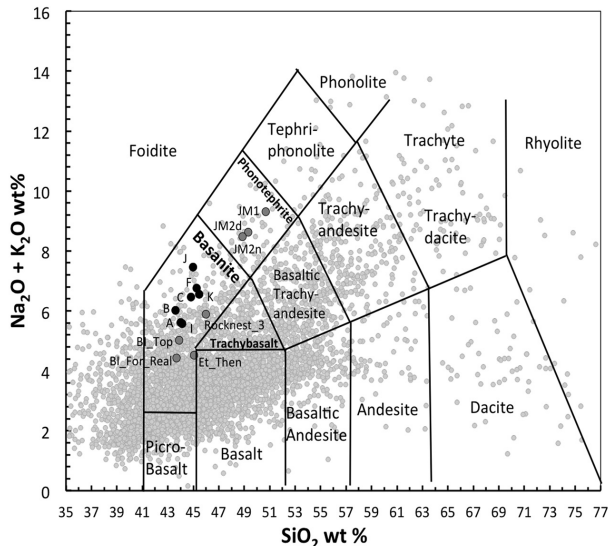
FIGURE 1. TAS diagram showing the composition of the 7 San Carlos rocks with varying degrees of aqueous alteration examined in this study. All samples plot in the basanite field with SiO$_2$ wt% between 44 and 44.5% and total alkali percentages between 5.6 and 7.4%. Dark gray circles show the composition of Jake Matijevic, Bathlet Inlet, Rocknest, and Et_Then from APXS analyses at Gale crater on Mars (Stolper et al. 2013). Smaller light gray circles show the compositions of all ChemCam analyses at Gale crater (up to August 9, 2015). Plotted ChemCam analyses were not filtered for igneous samples, and the distribution of points exhibits the compositional diversity of igneous float rocks and the igneous protoliths sampled by sedimentary rocks.

on subalkaline basalts (e.g., Golden et al. 2005; Hurowitz et al. 2005; Hurowitz and McLennan 2007; Hausrath et al. 2008; Ehlmann et al. 2012; Greenberger et al. 2012). Few analog studies of alkaline basalts exist, but these have become relevant to the interpretation of returned data, given the finding of Spirit and Curiosity rovers, as described above. Thus, there are two goals of this work: (1) the study of aqueous alteration of specifically alkaline basalts as Mars analogs, and (2) the collection of laser-induced breakdown spectroscopy (LIBS) data of well-characterized and Mars-relevant samples to improve the ability of ChemCam to quantify elemental composition and identify signs of aqueous alteration in minerals and soils at Gale Crater. For the latter objective, ChemCam uses a partial least squares (PLS) approach to determine the geochemistry of martian rock samples based on a library of known standards (Clegg et al. 2009; Wiens et al. 2013). PLS works best when the library samples closely match the composition of materials being observed (Clegg et al. 2009, 2014, 2016). Hence, the rocks described and characterized here were used to supplement others to create a new >400 sample database (Clegg et al. 2014, 2016) from the previous library size of 72 (Wiens et al. 2013). Here we focus on the first goal, which is the study of aqueous alteration of specifically alkaline basalts as Mars analogs.

We used multiple laboratory techniques to characterize a suite of 2–3 Myr basalt flows from San Carlos, Arizona. Waters had interacted with the samples, causing oxidative weathering and some clay formation. Samples collected from the flows

exhibited a range in alteration extent and/or style, indicated to first order by varying amounts of reddish-brown material on the rock surface, extending into the interior. The San Carlos suite was chosen as an analog for alteration of alkaline basalts on Mars due to the similarities in original rock lithology and the fact that alteration appeared to be minor. The semi-arid environment is likely warmer than that at the Mars surface, thus speeding reaction kinetics, but the relatively small degree of alteration offered the chance to study in detail the early stages of chemical breakdown of an alkaline basalt. Visible and short-wave infrared (VSWIR) spectra, X-ray diffraction (XRD), bulk chemistry, and electron microprobe data were collected from this suite of basalts. The data was used to identify all primary minerals and their compositions, estimate bulk composition and mineralogy, characterize alteration by identifying various minerals and alteration reactions, and provide information on past weathering processes, as well as primary compositions. Following sample characterization, the San Carlos basalt suite was measured by LIBS, in both whole-rock and compressed pellet forms, for addition to the ChemCam library (Ehlmann et al. 2013; Clegg et al. 2014, 2016). Here, using the suite of techniques, we determine the primary and secondary mineralogy and chemical alteration pathways of the San Carlos rocks.

Geologic setting and samples

Six of the seven samples were collected from the San Carlos ultramafic inclusion locality, in Peridot Canyon, San Carlos, Arizona (Fig. 2). Peridot Mesa, incised by the canyon, is composed of late Tertiary or early Quaternary basalt flows. One sample was purchased from the same locality to obtain a pristine, least weathered rock and may be from a slightly different locale than the rest of the suite. Bright green ultramafic xenoliths, largely olivine, are widespread throughout the locality, occurring as large gravity-settled masses in the basaltic flows. The host rock is fine-grained and consists of plagioclase laths with smaller grains of pyroxene, nepheline, leucite, and titanomagnetite; small olivine xenocrysts are also present (Frey and Prinz 1978). All samples exhibit various degrees of weathering as evidenced by differences in color and reaction boundaries between the host rock and xenolith. Highly altered basalts appear rust-colored, whereas less altered basalts appear gray. The rust-colored texture on the exterior of the rock was analyzed in thin sections and identified as a rind, which we define as an alteration horizon with a gradation from altered to more pristine material. In contrast, coatings are deposited from external sources, and are discontinuous with the surface of the rock (Salvatore et al. 2013). Only sample F has an identifiable coating of gypsum. The size of each sample varies from about a quarter of a meter to fist-sized (Fig. 2). For this work, we focus on the basaltic host rock, rather than the olivine-rich xenoliths.

Methods

VSWIR spectral measurements

The suite of basalts was labeled and photo-documented under normal lab conditions. Also, written descriptions of each rock were made prior to further analysis. The suite of sample rocks was then measured under ambient lab conditions using an Analytical Spectral Devices (ASD) spectrometer with a contact probe attachment to obtain visible and short-wave-infrared reflectance spectra from 0.4 to 2.5 μm. Spectra were calibrated to reflectance using a Spectralon
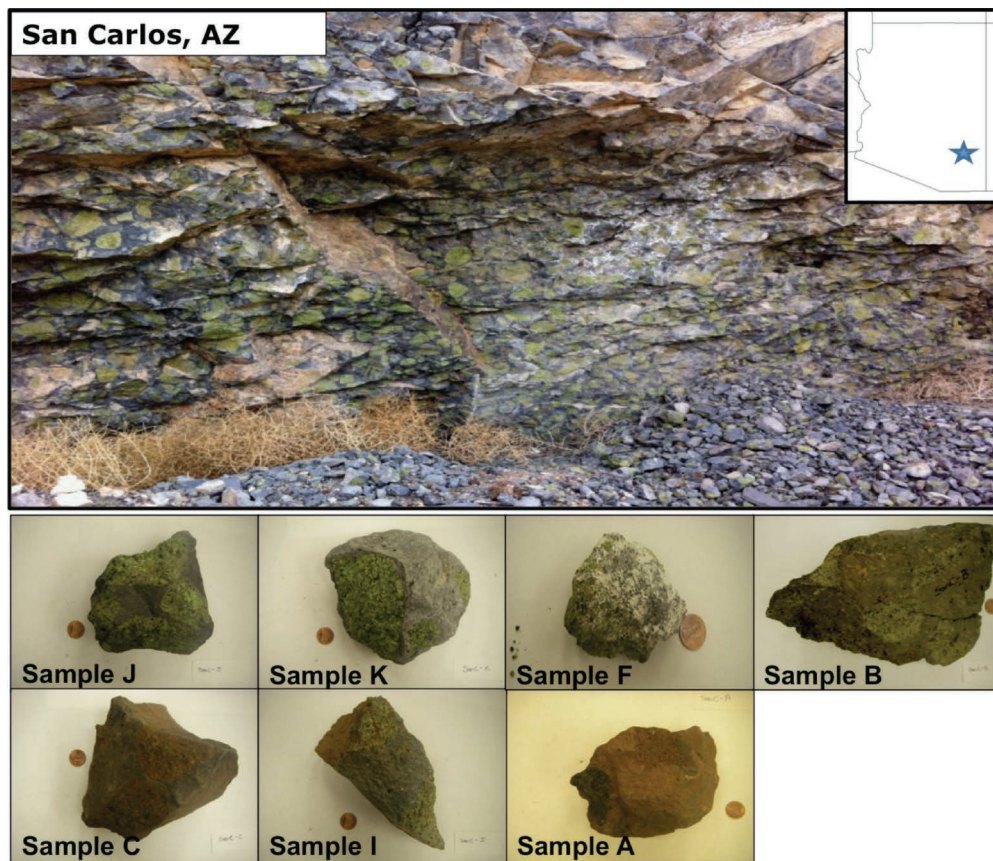
FIGURE 2. (**upper**) Location of the San Carlos Peridot Mesa in San Carlos, Arizona, and an outcrop of basalt with olivine xenoliths. (**lower**) Basalts ordered from least to most altered based on visual appearance. Sample J = least-altered basalt with bright green olivine xenoliths. Sample K = relatively pristine basalt. Sample F = relatively pristine basalt with gypsum coating. Sample B = intermediately altered basalt with friable olivine xenoliths Sample C = intermediately altered basalt with red-brown olivine xenoliths. Sample I = highly altered red-brown basalt with friable olivine. Sample A = most altered red-brown basalt with reddish olivine xenoliths. (Color online.)

reflectance standard. Data were acquired from multiple surfaces on each rock to assess sample heterogeneity.

The spectral continuum, i.e., overall shape, is an indicator of the style and degree of alteration. Changes in overall continuum shape from flat to downward sloping to curved and concave down are related to the style and intensity of rock alteration. Negative slopes between 0.75 and 1.0 μm indicate NIR "blue" slopes (decreasing reflectance with increasing wavelength); positive slopes between the same range indicate NIR "red" slopes (increasing reflectance with increasing wavelength) (e.g., Farrand et al. 2006). In terms of styles of alteration, an overall concave down slope over the 0.4–2.5 μm range, i.e., initially increasing reflectance then decreasing reflectance with increasing wavelength, suggests the presence of Fe^{3+} oxides and strong UV/visible absorptions to create the initial upward continuum slope to ~1.5–2.0 μm and hydrated silicates with strong 3 μm H_2O- and OH-related absorptions that create the downward sloping continuum to longer wavelengths. In contrast, an overall negative slope (for basaltic materials) suggests a coating or powder obscuring the surface, possibly a thin coating of silica (e.g., Mustard et al. 2005; Minitti et al. 2007; Skok et al. 2010), and the underlying rock need not be significantly altered.

The spectra were also examined for absorptions due to primary and secondary minerals. Broader features nearer 1.0 μm and from 1.8–2.2 μm are due to electronic transitions of Fe^{2+} in pyroxenes. Features centered at 1.0 and 2.2 μm indicate high-Ca pyroxenes, whereas broad absorptions at 0.90 and 1.90 μm indicate low-Ca pyroxenes (Sunshine and Pieters 1993). Iron oxides have absorptions in the UV region and near 0.9 μm. Steep positive slopes at wavelengths <0.50 μm and from 0.6 to 0.8 μm indicate the presence of ferric iron oxides, which are weathering products; long wavelength features near 0.9 μm also indicate well-crystalline ferric iron oxides. Hematite is distinguished by an electronic transition at 0.86 μm.

Goethite has a similar feature between 0.9 and 0.93 μm (Morris et al. 2000). Phyllosilicates and clay mineralogy are indicated by a combination of OH stretching and metal-OH bending between 2 and 2.5 μm. Absorptions near 2.2 μm indicate Si-OH or Al-OH in phyllosilicates and opaline silica. For Al-rich clays such as montmorillonite, the Al-OH absorption occurs at 2.21 μm and is sharper than the Si-OH absorption in silica. Fe-OH is indicated by absorptions near 2.29 μm, and absorptions around 2.31 μm indicate Mg-OH. An absorption near 1.9 μm indicates an H-O-H bend and OH stretch caused by the presence of molecular H_2O in clay interlayers (Bishop et al. 1994). Bands near 1.4 μm indicate the first overtone of the OH stretch and H_2O combinations (Bishop et al. 2008; Clark et al. 1990, 2007a).

Band depth calculations for the 0.53, 1.9, 2.2, and 2.3 μm absorptions in host basalt spectra were determined using ENVI. Spectra were continuum-removed, and the absorption of each identified band was measured by manually finding the band center in the continuum-removed spectra. In this work, we used the CRISM defined band parameters BD530, BD1900, BD2210, and BD2290 to measure continuum-removed band strengths (Pelkey et al. 2007). Quantification of these band depths provides information on relative water content, ferric iron content, and metal-hydroxide content.

Preparation for geochemical analyses

After spectral measurements were taken, a subset of samples was chosen based on diversity in types of aqueous alteration, weathering products, and degree of alteration, as evident from both the spectral properties and visual analysis. A small portion of each sample within the subset was selected for preparation of polished thin sections, impregnated with epoxy, and allowed to cure overnight. The purpose of the epoxy impregnation was to preserve any coatings or alteration rinds present on the rock, which affect VSWIR spectral properties and would otherwise have

been washed away or abraded during thin section preparation. Locations of thin-section cuts were selected to include a wide variety of minerals, each representing the different spectral classes of materials. Ideal portions contained surfaces and interior portions of both host rock and xenoliths, thought only the host rock is the focus of this study. The intent of the thin-section analysis was to determine the chemical composition of mineral phases present and to examine textural relationships between primary and secondary minerals.

The San Carlos host rocks were also analyzed for bulk-chemical composition (major, minor, and trace elements). Rocks were somewhat heterogeneous from visual indicators of aqueous alteration, so representative parts of the host rock of each sample that did not have an alteration rind and that lacked xenoliths were chipped off using a rock hammer and chisel or rock saw. The intent of the bulk-rock measurement was to compare the chemistry across rock samples and to test for trends corresponding to degree of alteration, measuring the composition and degree of alteration of the basalts only, not xenoliths, and leaving analysis of any potential rinds for microprobe work.

Bulk-chemical analysis

Bulk-chemical analysis was performed by Activation Labs, Ltd., in Ontario, Canada. Bulk-rock chips were powdered and mixed with Li metaborate and Li tetraborate flux in graphite crucibles. The mixture was fused in a furnace at 1150 °C and the resulting fused material was dissolved in a mixture with 5% nitric acid. Fused samples were then diluted and analyzed with Perkin Elmer Sciex ELAN 6000, 6100, or 9000 ICP/MS. For every group of samples, three blanks, three controls before the sample group, and two blanks after the sample group were run. Duplicates were analyzed after every 15 samples and the instrument was calibrated every 40 samples. Total Fe is reported as Fe_2O_{3T} for these data because of oxidation during the fusion process.

Electron microprobe

The thin sections were first observed using a petrographic microscope to survey rock textures and alteration and to identify areas of interest. The host rock (basanite) is composed mainly of fine-grained pyroxene, plagioclase, and olivine. Xenoliths are almost entirely composed of coarse-grained olivine with some pyroxene and opaque minerals. Samples were then placed in a vacuum carbon evaporator and coated with a thin layer of conductive carbon. Electron microprobe measurements were done with the JEOL JXA-8200 at Washington University in St. Louis. Measurements were made using a 15 KV accelerating potential, 25 nA beam current, and a range of beam sizes from 1 to 10 μm, depending on the grain size and the susceptibility of a grain to volatilization. Both reflected light and backscattered electron imaging were used to search for textures caused by alteration and to focus the beam for analyses of elemental abundances. Energy-dispersive spectrometry (EDS) was used to identify mineral phases and to guide subsequent quantitative analyses.

Quantitative analyses were done using the five wavelength-dispersive spectrometers and a combination of diffracting crystals for two to four elements, as follows: Na, Mg, Al, and Si were analyzed using the TAP crystal; Mn, Fe, and Si were analyzed using the LIF crystal; Ti and Cr were analyzed using LIFH; and S, K, and Ca were analyzed using PET. Elemental standards used were Amelia Albite P-103 (Na), Shankland synthetic Forsterite P-658 (Mg), Alaska Anorthite NMNH 137041 (Al), Gates Wollastonite (Si and Ca), Madagascar Orthoclase GRR78 (K), Mn Olivine RDS P-1087 (Mn), Fe_2O_3 Elba Hematite P-238 (Fe), TiO_2 GRR (Ti),

and Cr_2O_3 P-585 (Cr). Quantitative analyses were done using Probe for EPMA software and X-ray corrections were done using the CITZAF correction software [Φ(ρz) algorithm; Armstrong 1995].

Because the microprobe does not distinguish Fe^{2+} and Fe^{3+}, total Fe concentrations are reported in terms of FeO. These values were converted to Fe_2O_3 for comparison with bulk-chemical analyses, for which total Fe was reported as Fe_2O_3. For magnetite and spinels, Fe_2O_3 values were adjusted for contributions from ferric oxide (Fe^{3+}) using stoichiometry. The fraction of Fe^{3+} to total iron was calculated by adjusting the fraction of Fe^{2+} to total iron until the sum of total cations was 3.00.

X-ray diffraction

Bulk-rock powders were placed into 3.8 cm by 5 cm fixed sample mounts and tamped down using a metal spatula to form a flat surface. X-ray diffraction (XRD) measurements were taken using the Bruker d8 X-ray powder diffractometer at Washington University in St. Louis using Cu$K\alpha$ radiation at a maximum power of 100W operating at 40 kV and 40 mA, with a 0.5 per second per step count time. Data was analyzed using the DIFFRAC.EVA and DIFFRAC.SUITE TOPAS software for Rietveld refinement. Rietveld refinements were performed automatically, using a peak-fitting algorithm with a library of standard minerals, and manually by selecting peaks of interest and identifying potential mineral candidates based on bulk-geochemical data.

## RESULTS

VSWIR spectral analysis

Diversity in spectral properties both among samples and within samples indicates differences in both weathering extent and the nature of weathering chemical processes affecting the rocks. For the host rock, key features were the variation in overall slope and continuum shape, the depth of absorption features related to ferric iron, and the depth or narrowness of vibrational absorption features at longer wavelengths (1.4 to 2.5 μm), indicating the presence of metal-OH and H_2O (Table 1; Fig. 3).

Continuum shape and slope. Overall continuum shape and slopes at longer wavelengths are indicators of the degree of alteration, as well as the style of alteration. Less-altered samples have an overall flat slope with few prominent absorption features. This pattern is typical for a relatively pristine basalt, which has an overall low albedo and shallow, broad features related to pyroxene around 1.0 and 2.0 μm. With increasing alteration, the overall continuum shape changes from flat to downward sloping (blue-sloped spectrum), e.g., samples B and F. Blue-sloped spectra can indicate surface coatings on basalts, and a gypsum coating was identified for sample F (Skok et al. 2010). As alteration progresses, the overall continuum shape becomes more curved and has a concave-down shape, common for spec-

TABLE 1. VSWIR determined mineralogy of all of the bulk-rock samples in order of increasing alteration determined by visual analysis (amount of red material on surface) and overall continuum shape; italicized entries are subset used for further study

Sample	Description	Overall continuum	Ferric absorptions (μm)	Vibrational Absorptions (μm)	VSWIR-determined mineralogy
SanC-J	large dark gray basalt	flat, constant slope	–	small 1.41; small, broad 2.21; small 2.31	hydrous Si + Fe/Mg clay
SanC-K	large mottled gray/light gray basalt	flat, constant slope	–	small 1.41; broad 2.21	hydrous Si
SanC-F	small gray basalt, white coating	downward slope	–	1.50; doublet at 1.95 and 2.04; 2.21	gypsum coating
SanC-C	large dark brown/rust basalt	curved, concave down	0.5, 0.53, pos. UV-Vis slope, 0.89–0.99	1.41; sharp and broad 2.21	hydrous Si + Al-smectite + Fe^{3+}-ox
SanC-B	massive gray/brown basalt	downward slope	0.5, pos. UV-Vis slope, 0.97	sharp 1.42, broad 2.21, 2.29–2.32	hydrous Si + Mg clay + Fe^{3+} oxide
SanC-I	large gray/rust-colored basalt	downward slope	sharp 0.53 band	1.41; 2.21 bands	Al-smectite + Fe^{3+} oxide
SanC-A	large basaltic rock, rust colored	curved, concave down	0.5, 0.53, pos. UV-Vis slope, 0.91	sharp 1.41 and 2.21 bands	Al-smectite + Fe^{3+} oxide

Notes: Note that all samples have 1.9 μm vibrational absorptions, so these are not listed.
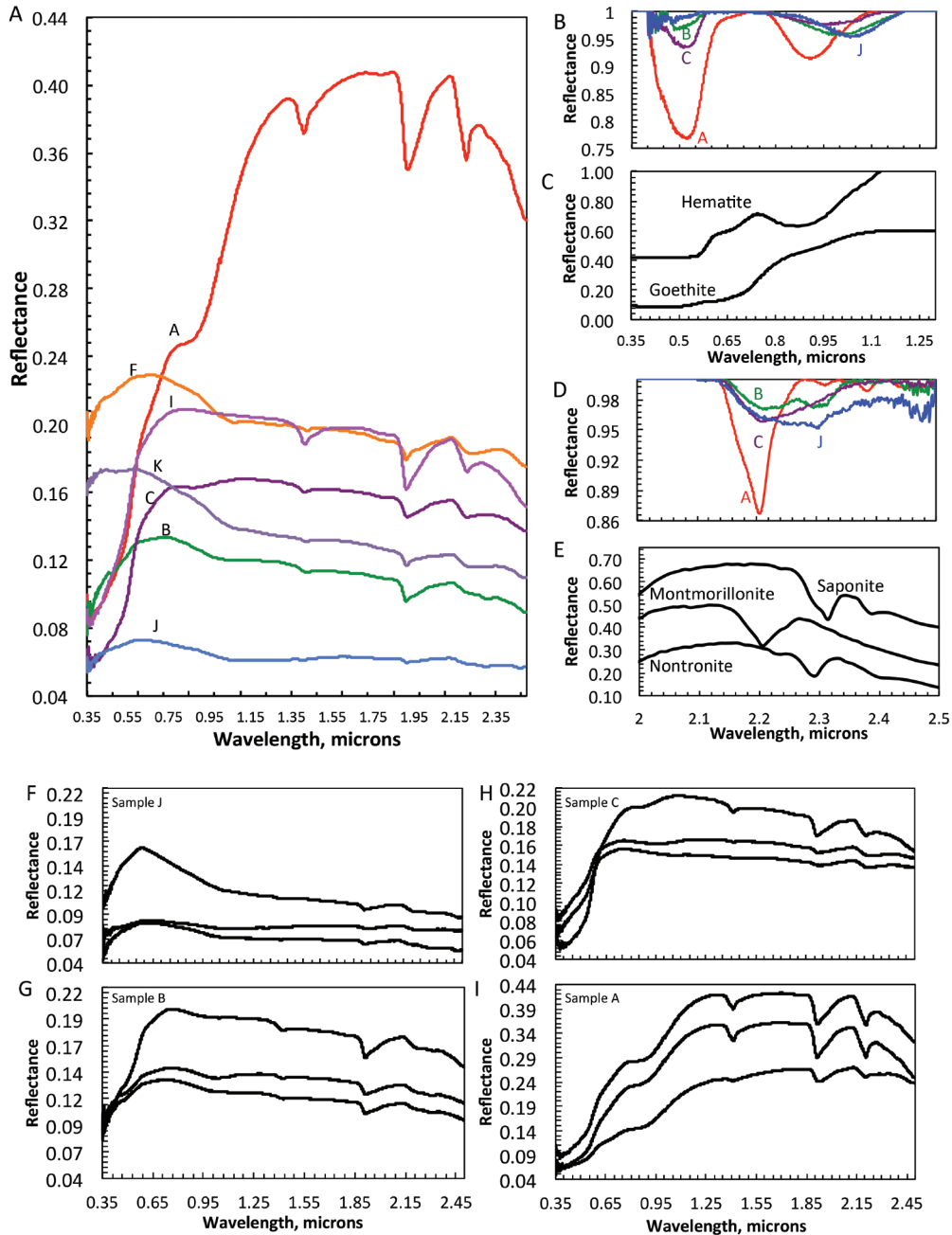
FIGURE 3. (**a**) Average spectra for all 7 samples; features at 0.53, 1.0, 1.4, 1.9, 2.2, and 2.3 μm were used to identify primary and secondary mineralogy in each sample. (**b**) Continuum removed end-member spectra of the 4 end-members (samples J, B, C, and A) between 0.35 and 1.35 μm. This region was used to identify ferric iron features near 0.5 μm, as well as ferrous iron features near 1.0 μm. (**c**) Reference spectra of iron oxides from the USGS Spectral Library (Clark et al. 2007a) between 0.5 and 1.3 μm. (**d**) Continuum removed end-member spectra of the 4 end-members (samples J, B, C, and A) between 2.0 and 2.5 μm. This region was used to identify metal-OH absorption features that are indicative of phyllosilicates; absorption bands at 2.2 and 2.3 μm are indicative of Si-OH or Al-OH and Fe-OH or Mg-OH, respectively. (**e**) Reference spectra of phyllosilicates from the USGS Spectral Library (Clark et al. 2007a) between 2.0 and 2.5 μm. (**f**) Spectral variability in sample J; key absorptions are at 1.9, 2.2, and 2.29–2.30 μm. (**g**) Spectral variability in sample B; key absorptions are at 1.9 and 2.31 μm. (**h**) Spectral variability in sample C; key absorptions are at 1.9 and 2.2 μm. (**i**) Spectral variability in sample A; strong absorptions are at 1.9 and 2.2 μm. (Color online.)

tra of altered materials due to ferric oxide absorption at shorter wavelengths and the leftward shoulder of the strong OH and H_2O absorptions from 2.7 to 3 μm. The samples I and A have

the most curved, concave-down overall continuum shape. Based on overall continuum shape and slope, samples are ordered, in terms of increasing alteration, from J, K, B, F, C, I, to A (Table 3).

TABLE 2. Band depth calculations and corresponding wavelength for all samples in order of increasing alteration determined by visual analysis and overall continuum shape; italicized entries are subset used for further study

Sample	SanC-J	SanC-K	SanC-F	SanC-C	SanC-B	SanC-I	SanC-A
Avg wavelength	1.915	1.912	1.914	1.918	1.9132	1.914	1.917
Avg BD1900	0.072	0.113	0.101	0.068	0.128	0.166	0.155
Avg wavelength	n/a	n/a	n/a	0.529	0.526	0.526	0.532
Avg BD530	n/a	n/a	n/a	0.127	0.096	0.169	0.273
Avg wavelength	2.299	2.312	2.316	2.315	2.312	2.309	2.312
Avg BD2300	0.029	0.005	0.003	0.003	0.163	0.002	0.005
Avg wavelength	2.208	2.214	2.214	2.207	2.207	2.206	2.204
Avg BD2200	0.0285	0.039	0.024	0.043	0.020	0.070	0.099

Note: The 1.9 μm band depth is an indicator of water content, and band depths at 2.2 and 2.3 μm indicate Al-OH and Fe,Mg-OH content (e.g., Milliken and Mustard 2005).

TABLE 3. Bulk-chemical analysis (wt%) for all samples in order of increasing alteration; samples selected for further analysis are italicized

Oxides	SanC-A	SanC-B	SanC-C	SanC-F	SanC-I	SanC-J	SanC-K
SiO_2	44.0	43.6	44.8	45.3	44.1	45.0	45.5
TiO_2	2.79	2.67	2.73	2.72	2.68	2.66	2.70
Al_2O_3	15.0	14.7	14.6	14.8	14.7	15.1	14.6
Cr_2O_3	0.00	0.00	0.00	0.00	0.00	0.00	0.00
Fe_2O_{3T}[a]	13.5	12.5	13.4	13.1	13.1	13.3	12.9
MnO	0.20	0.19	0.20	0.20	0.20	0.20	0.20
MgO	8.03	7.80	9.04	8.35	7.79	7.40	8.08
CaO	7.90	7.74	7.66	7.64	7.73	7.38	7.58
Na_2O	3.34	4.86	3.92	5.27	4.30	4.62	5.27
K_2O	2.27	1.16	2.55	1.48	1.28	2.84	1.28
P_2O_5	0.75	0.73	0.77	0.79	0.85	0.86	0.85
Total	97.0	95.2	98.9	98.8	95.8	98.4	98.1
Loss	3.0	4.8	1.1	1.2	4.2	1.6	1.9
$CaO+Na_2O+K_2O$	55.25	56.21	56.4	58.16	56.16	56.97	58.32
Na_2O+K_2O	5.61	6.02	6.47	6.75	5.58	7.46	6.55

[a] All Fe is reported as Fe_2O_{3T}.

Fe-related absorptions. Indicators of ferric iron are absorption features at 0.53 and ~0.9 μm, as well as slopes between 0.6 and 0.8 μm. Relatively pristine basalts have shallow bands at 0.53 μm and broad, shallow bands at ~0.9 μm, related to Fe^{3+} electronic transitions in crystalline Fe-oxides. The depths of both of these bands are related to ferric iron content, and increase with increasing alteration; sample A has a strong absorption feature at 0.53 μm and a sharp band at 0.91 μm. Slopes between 0.6 and 0.8 μm also indicate the presence of Fe-oxides. Samples J and K have a negative slope between 0.6 and 0.8 μm, suggesting little to no ferric iron content, whereas samples I and A have steep positive slopes in this same region, suggesting greater ferric iron content with increasing alteration. On the basis of the band depth at 0.53 μm (BD530), samples are ordered in terms of increasing ferric iron content from J, K, B, F, I, C, to A.

H_2O and metal-OH absorptions. Absorption features at 1.9 μm are an indicator of H_2O in clay interlayers, hydrated silica, or other hydrous phases and should increase with alteration and sample weathering. In the San Carlos samples, increasing BD1900 is correlated with BD530, suggesting a relationship between water and ferric iron content (Fig. 4). All samples contain bands at 1.4 μm of varying depths, related to hydroxyls in hydrated silicates and molecular water; these features are small and shallow in J and K samples, and increase in depth for C, I, and A samples.

Absorption features at longer wavelengths indicate the presence of hydrated silicates. The depth and position of absorption features at longer wavelengths varies significantly between samples, indicating changes in Al-OH and Fe,Mg-OH content (Table 2). Less-altered samples (J and K) have broad, shallow absorption features near 2.2 μm, indicating Si-OH possibly due to the presence amorphous silica or poorly crystalline silicate weathering products. More-altered samples have sharper absorption features at 2.2 μm, indicating Al-OH and/or weak, broad features at 2.29 or 2.3 μm, indicating Fe or Mg-OH. Sample B has a both a broad absorption feature at 2.2 μm due to Si-OH and a sharp feature at 2.3 μm, indicating greater Fe/Mg-OH-bearing phase content compared to other samples. Samples A and I have strong, sharp absorption features at 2.2 μm and weaker bands at 2.3 μm, suggesting more crystalline Al clays, or greater Al-OH content compared to Mg-OH content. BD2210 (Al-OH or Si-OH) increases with BD1900 (water content) and BD530 (ferric iron content) for all samples, suggesting a trend in alteration with increasing and correlated Si-OH/Al-OH and ferric iron as alteration progresses. BD2290 (Fe-OH) varies little with other spectral parameters and only one sample (B) has a BD2290 value above 0.03 (Table 3; Fig. 4).

From the initial suite of seven rocks, four spectral end-members were identified on the basis of these three classes of spectral parameters. J appears to be the least altered sample with an overall flat continuum shape, weak ferric absorption features, and broad features at 2.2 μm. B is an intermediately altered basalt, and has a blue-sloped spectrum, a weak band at 0.53 μm, broad features at 2.2 μm, and a sharp feature at 2.3 μm. C is also an intermediately altered basalt but with a slightly curved, concave-down continuum shape and small, sharp features at 0.53 and 2.2 μm. Sample A is the most altered sample with a curved, concave down overall shape and very sharp absorption features at 0.53 and 2.2 μm. These 4 samples represent a different extent and/or style of weathering, and their thin sections were analyzed in detail with the electron microprobe.

Bulk-chemical analysis

Results from bulk-chemical analysis are given in wt% oxide for all seven samples, along with calculated normative mineralogy (Table 4). Totals range from 95.2 to 99.1% with differences due to loss on ignition and slight variations in Fe^{2+}/Fe^{3+}. Variations in weight percents for individual oxides are minimal, with the most variation in Na_2O (3.34 to 5.27%). Bulk-rock compositions fall within the basanite field on a TAS diagram (Fig. 1). Sample J has a slightly higher alkali content (7.46%) compared to all other samples. In contrast, sample Sample A, has a slightly lower alkali content (5.61%) relative to other samples. From bulk-chemical data, normative mineralogy for each sample was calculated by the CIPW normative method. The San Carlos samples have less silica and alkalis than the Jake M rock at Gale crater (Stolper et al. 2013) and are most comparable to the Wishstone class at Gusev crater (McSween et al. 2006), albeit slightly lower in magnesium and iron.

Electron microprobe analysis

The four spectral end-members were analyzed using backscattered electron imaging and spot analyses to look for primary and alteration textures and determine mineral compositions. Key findings were distinct textures for olivine, titanomagnetite, and
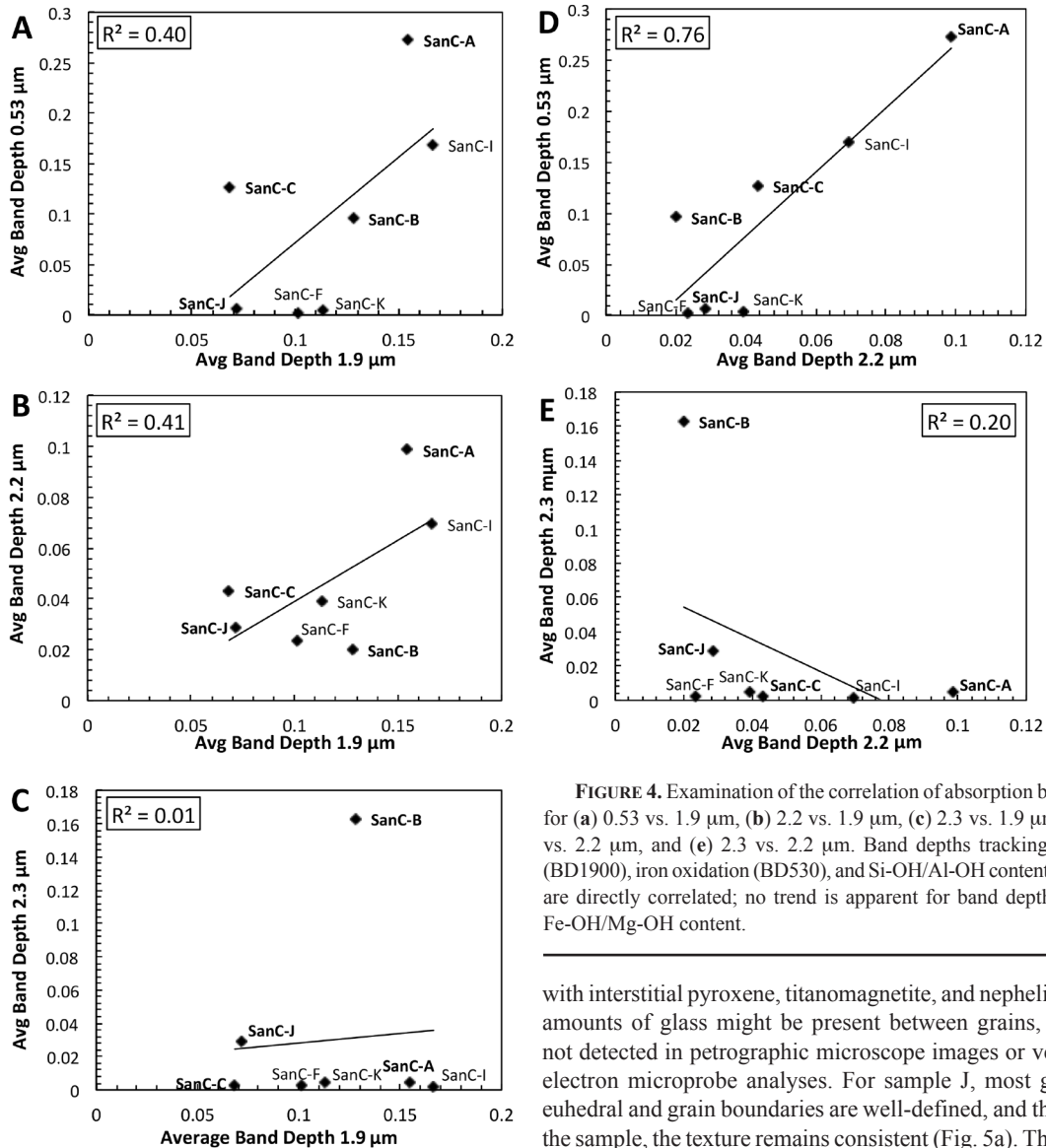
FIGURE 4. Examination of the correlation of absorption band depths for (**a**) 0.53 vs. 1.9 μm, (**b**) 2.2 vs. 1.9 μm, (**c**) 2.3 vs. 1.9 μm, (**d**) 0.53 vs. 2.2 μm, and (**e**) 2.3 vs. 2.2 μm. Band depths tracking hydration (BD1900), iron oxidation (BD530), and Si-OH/Al-OH content (BD2200) are directly correlated; no trend is apparent for band depths tracking Fe-OH/Mg-OH content.

plagioclase laths, compositional ranges for various minerals, and evidence for alteration on the micrometer scale.

Overall textures and mineral assemblages. All samples have an overall porphyritic texture with larger olivine phenocrysts set in an intergranular matrix of plagioclase laths with interstitial pyroxene, titanomagnetite, and nepheline. Small amounts of glass might be present between grains, but were not detected in petrographic microscope images or verified by electron microprobe analyses. For sample J, most grains are euhedral and grain boundaries are well-defined, and throughout the sample, the texture remains consistent (Fig. 5a). The mineral assemblage consists of plagioclase, high-Ca pyroxene (augite), nepheline, and titanomagnetite, with zoned olivine phenocrysts. Samples B and C consist of the same mineral asssemblage, with the exception of zoned titanomagnetite in B, which is not present in C (Figs. 5b and 5c). For sample A, the overall texture in the interior of the section was similar to that for the pristine sample;

TABLE 4. Normative mineralogy calculated using the CIPW method from bulk-chemical analysis

Mineral	SanC-A	SanC-B	SanC-C	SanC-F	SanC-I	SanC-J	SanC-K
Feldspar	38.92 (32)	36.99 (24)	29.01 (29)	33.29	41.92	26.29 (31)	36.31
Orthoclase	14.25 (0)	7.50 (8.5)	15.55 (3.5)	9.10	8.22	17.38 (0)	8.05
Nepheline	5.24 (12)	11.69 (12)	10.28 (12)	12.85	7.06	13.53 (23)	11.47
Leucite	0.00 (10)	0.00 (10)	0.00 (7)	0.00	0.00	0.00 (0)	0.00
Hi-Ca pyroxene	10.50 (19)	16.19 (18)	14.81 (22)	16.43	13.46	15.46 (21)	16.24
Olivine	17.17 (12)	14.61 (10)	17.06 (11)	15.11	15.77	14.00 (13)	14.72
Ilmenite	5.47 (0)	5.32 (1.5)	5.22 (0)	5.22	5.30	5.11 (0)	5.22
Magnetite	6.08 (7)	5.70 (7.5)	5.86 (10)	5.76	5.92	5.84 (13)	5.70
Hematite	0.00 (4)	0.00 (5)	0.00 (5)	0.00	0.00	0.00 (2)	0.00
Total	99.55	99.82	99.73	99.76	99.82	99.77	99.81

Notes: Modal mineralogy (in parentheses) calculated by combining averages of measured mineral compositions from microprobe spot analyses and phase proportions from Rietveld refinement of bulk-compositional XRD data.
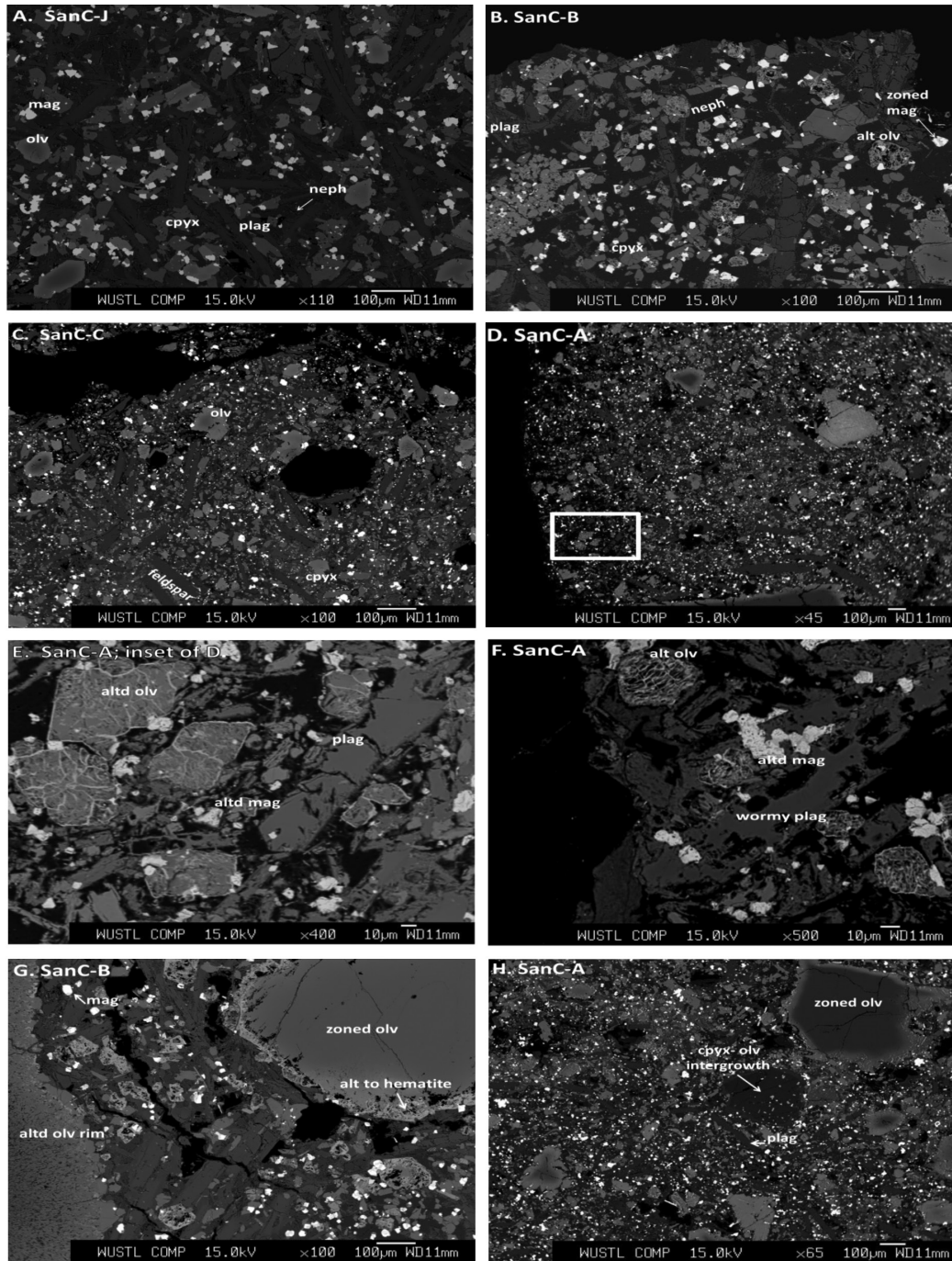
FIGURE 5. Backscattered electron images of alteration textures. (**a**) Unaltered primary minerals in SanC-J; lath-shaped grains are feldspar, dark interstitial phases are nepheline. (**b**) Wormy olivine textures from replacement by hematite veins in SanC-B; mottled, plagioclase dissolution texture in upper left and lower right. (**c**) Unaltered minerals on SanC-C near the sample edge. (**d**) Low-magnification image of SanC-A edge; white square is **e**. (**e**) Olivine altered to contain hematite veins, mottled titanomagnetite, and mottled feldspar laths. (**f**) Different edge in SanC-A showing similar textures to **d**. (**g**) Area around altered olivine rim in SanC-B. (**h**) BSE image in SanC-A interior showing an overall texture similar to that in SanC-C (**b**).

toward the rock exterior, most of the grains are subhedral, while the grain boundaries are poorly defined and appear frayed or ragged (Figs. 5d, 5e, and 5f). In Sample B, grain boundaries at the rock exterior also appeared frayed (Fig. 5g). The mineral assemblage for the Sample A consists of mottled plagioclase, high-Ca pyroxene (augite), nepheline, leucite, and titanomagnetite intergrown with an ulvöspinel phase, with olivine phenocrysts, some of which have been partially altered to poorly crystalline hematite or other iron-enriched phases (Fig. 5h).

**Compositions by mineral.** Olivine phenocrysts have com-

positions between Fo_{90} and Fo_{60} (Fig. 6). For sample (J) olivine compositions cluster around Fo_{90} with only a little zoning with higher Fe near the rim. More altered samples contain mixtures of olivine and hematite or another iron oxide from olivine alteration/oxidation. Possibly, olivine dissolution with removal of Mg^{2+} and oxidation of FeO to Fe_2O_3 is responsible for the variably high-iron olivines in more altered rocks. Pyroxene is mostly high-Ca pyroxene (Fig. 7). Most compositions plot in the augite field, with several compositions falling in the pigeonite and enstatite fields.

Opaque mineral compositions plot between Ti-hematite (ilmenohematite) and titanomagnetite in solid solution with ulvöspinel (Fig. 8). Sample J contains only titanomagnetite with no ulvöspinel phase. Sample A contains a wormy intergrowth of ulvöspinel and titanomagnetite partially oxidized to ilmenohematite. Sample C contains pristine titanomagnetite or titanomagnetite with distinct zones of exsolved ulvöspinel.

Feldspar compositions mostly lie in the plagioclase field between An_{30} and An_{70} (Fig. 9). Sample J, has an average plagioclase composition of $An_{56.5}Ab_{42}Or_{1.5}$. Samples B and C have average compositions of $An_{50}Ab_{48}Or_2$ and $An_{49}Ab_{49}Or_2$, respectively. Sample A has an average plagioclase composition of $An_{54}Ab_{44}Or_2$. A few compositions fall within the alkali feldspar field (compositions on average are ~$An_{21}Ab_{63}Or_{16}$). These compositions are alkali-rich edges from zoning of plagioclase in the primary melt. Both samples B and C contained zoned feldspars, with the average alkali-rich rim composition of $An_2Ab_{46}Or_{52}$ in B and $An_5Ab_{47}Or_{48}$ and $An_5Ab_{75}Or_{20}$ in C. Feldspathoids fall into two groups, nepheline or leucite, and occur as distinct grains between plagioclase laths or as individual grains near clusters of plagioclase laths. Nepheline is present in all samples, whereas leucite only occurs in samples C and A. Leucite compositions approach end-member $KAlSi_2O_6$, while nepheline compositions vary between samples. J has an average nepheline composition of $Ne_{71}Ks_6An_1Qz_{21}$; Samples A, B, and C have average nepheline compositions of $Ne_{68}Ks_6An_2Qz_{23}$, $Ne_{71.5}Ks_{6.5}An_{1.1}Qz_{20.6}$, and $Ne_{68}Ks_6An_{11}Qz_{14}$, respectively.

Evidence of phyllosilicates is found in samples A and B (Fig. 10). Phyllosilicates in sample A occur between plagioclase laths, along the rims of altered olivine grains, and between plagioclase and augite crystals. Most of these materials analyzed with the electron microprobe have wt% oxide totals between 80% and 89% suggesting that they contain a significant amount of OH or H_2O. For sample A, the most phyllosilicate-like compositions were found between plagioclase laths. In the sample B, most phyllosilicate-like compositions were found around altered olivine rims or between altered olivine rims and plagioclase laths. Spot analyses between plagioclase laths revealed more montmorillonite-like compositions. Analyses between altered mafic minerals revealed compositions similar to saponite, other Fe/Mg smectites, and chlorite (Fig. 10).

Primary and secondary textures. Primary textures for olivine phenocrysts are euhedral crystals with angular boundaries, best seen in sample J. There is some zoning but compositions are overall Mg-rich (Fig. 5a). In samples A, B, and C, olivine grains are zoned and many have a veiny texture along the edges or through the grain, representing olivine altered to hematite or another Fe^{3+} oxide (Figs. 5b–5h). Primary plagioclase and alkali feldspars, identified from sample J, are elongated laths with well-defined grain boundaries (Fig. 5a). Feldspar laths in
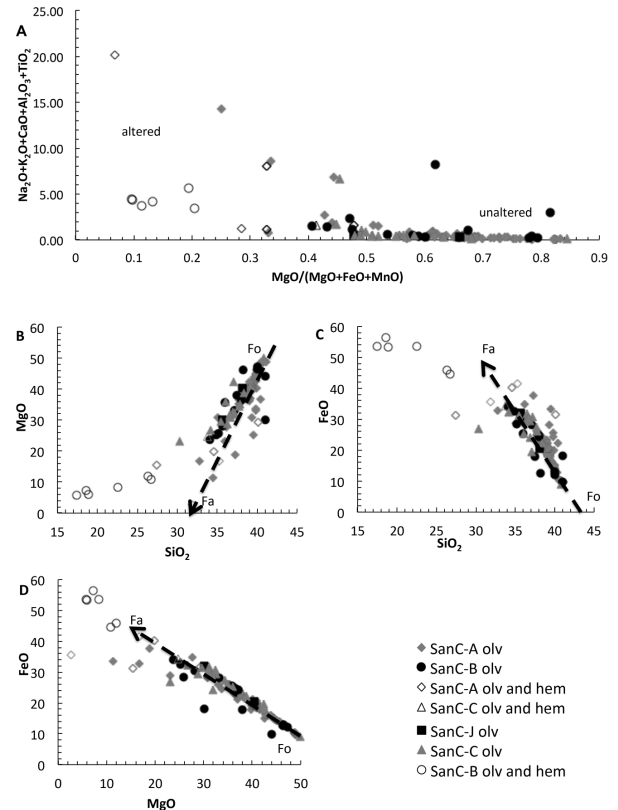

FIGURE 6. (**a**) Mg# (Mg over the sum of MgO, MnO, and FeO) vs. Na, K, Al, Ca, and Ti oxides for olivine (in wt%) calculated on the basis of four oxygen atoms from microprobe analyses. As described in the text, the observed compositional variation is partly primary and partly an effect of alteration. (**b–d**) Weight percent oxide plots from microprobe analyses of olivine grains (hem = hematite). (**b**) MgO vs. SiO_2 wt%; deviations from the Fo-Fa line represent alteration, primarily in the formation of veinlets of hematite. (**c**) FeO vs. SiO_2 wt%; variation along the Fo-Fa line indicates changes in composition from olivine grain Mg-rich cores to more Fe-rich rims, a primary compositional variation. (**d**) Primary variance in MgO and FeO from magnesian cores to ferroan rims; deviations from the Fo-Fa line and FeO enrichment indicate the occurrence of hematite veining in more Fe-rich rims.
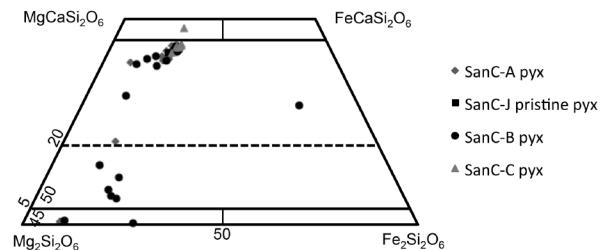
FIGURE 7. Composition of pyroxene (in mol%) calculated on the basis of six oxygen atoms, as determined by electron microprobe analyses of thin sections; most pyroxenes plot in the augite and pigeonite fields.

A, B, and C have a range of textures from mottled or wormy on the rock exterior to fairly pristine in the rock interior (Figs. 5b, 5c, and 5e). Highly irregular, wormy feldspar laths are present
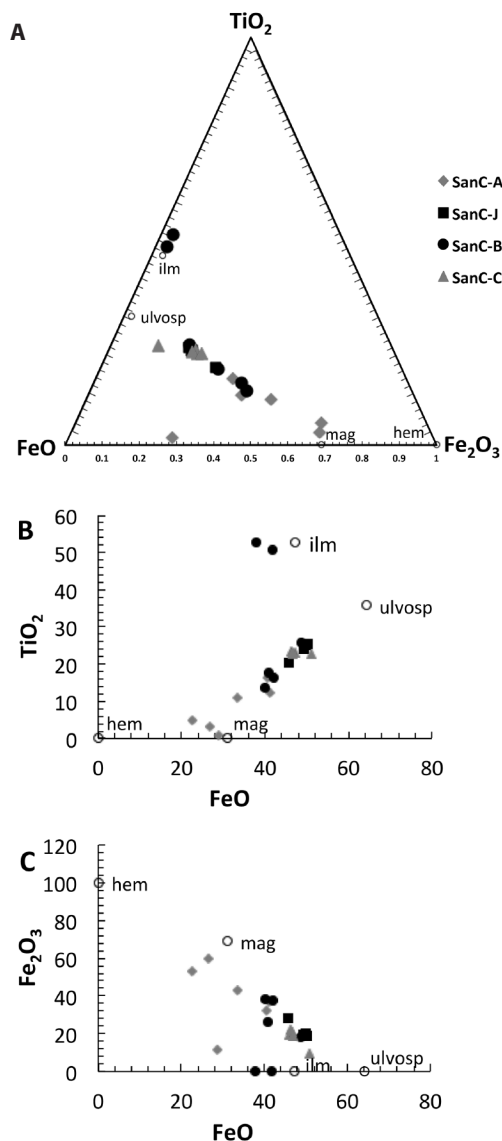
FIGURE 8. Weight percent oxide plots from microprobe analyses of opaques (ulvosp = ulvöspinel $TiFe_2^{2+}O_4$; mag = magnetite $Fe^{2+}Fe_2^{3+}O_4$; hem = hematite $Fe_2^{3+}O_3$, ilm = ilmenite $Fe^{2+}TiO_3$) calculated on the basis of four oxygen atoms. (**a**) Composition of Fe-Ti oxides from electron microprobe analyses, (**b**) Most of the oxide compositions fall along a join between ulvöspinel and Ti-rich magnetite. (**c**) More altered samples also trend toward hematite as titanomagnetite is oxidized.

in sample A only (Figs. 5e and 5f). Primary augite is euhedral with angular boundaries for all samples, and no alteration textures for pyroxene were found. Titanomagnetite in sample J occurs as bright, distinct grains with well-defined grain crystal boundaries (Fig. 5a). Other samples contain pristine titanomagnetite textures (C) and intergrown titanomagnetite and ulvöspinel (possibly exsolved; B) (Figs. 5b and 5c). Secondary alteration textures for titanomagnetite occur only in the sample A, where titanomagnetite crystals have a mottled, wormy texture with some irregularly shaped, distinct spinel zones (Figs. 5e and 5f).

XRD analysis. Using both an automated peak fitting algo-
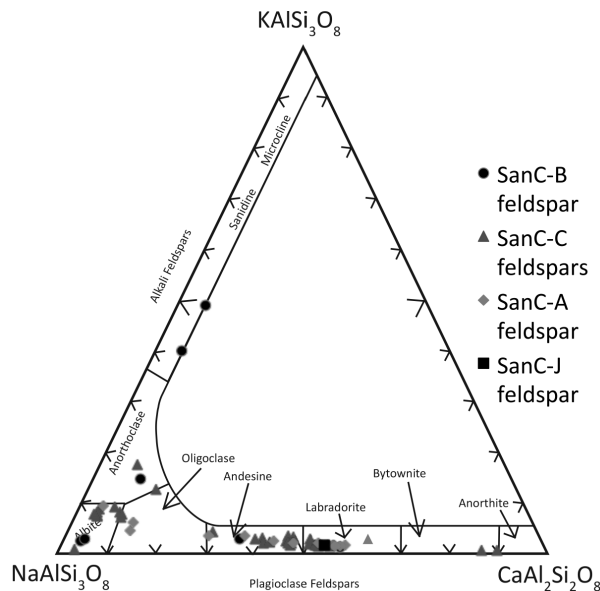
FIGURE 9. Composition of feldspars (in mol%) calculated on the basis of 8 oxygen atoms, as determined by electron microprobe analyses; most feldspars plot in the plagioclase field with the exception of a few analyses of alkali feldspar rims in SanC-B and -C.

rithm and manually selected peaks for inclusion in the Rietveld refinement model, we identified mineral assemblages and the percentages of each mineral for every sample. The resultant mineral suites are in agreement with the assemblages identified by our normative mineralogy analysis of the bulk-chemical data (Figs. 11a–11b; Table 4). Phyllosilicate peaks were not directly detected at low-2θ but phyllosilicates identified in VSWIR spectra and microprobe images were also included in Rietveld refinements.

Forward modeling. We combined the percentages of minerals identified by Rietveld refinement with the average mineral compositions obtained from electron microprobe point analyses to obtain total oxide abundances. All of the phases identified by Rietveld refinement were listed, and, when available, the average composition (in terms of oxide weight percentages) from electron microprobe spot analyses was assigned as the "true" composition for each mineral. Each oxide wt% was weighted by the percentage determined through the Rietveld refinement analysis. These percentages were then adjusted to closely match the bulk-oxide weight percentages with the bulk-chemical analysis data, minimizing residuals (Tables 3 and 4). Most of the minerals detected in the XRD data set were also identified in electron microprobe images and analyzed by direct spot analyses. Also, the relative order of the most abundant primary minerals in XRD (arranged from most to least abundant) is in agreement with the normative mineralogy calculations and visual analysis of petrographic microscope images. For the primary minerals, the order from most to least abundant is: plagioclase, augite, olivine, nepheline, and ulvöspinel/titanomagnetite (Table 4).

DISCUSSION

Results from VSWIR spectra suggest multiple weathering products and evidence for the formation of ferric oxides,

crystalline to poorly crystalline phyllosilicates, and amorphous silica coatings or weathering products in varying amounts for all samples. Results from bulk-chemical analysis indicate weathering is modest and largely isochemical with little changes in oxide wt% totals between individual samples, except for 1–2% alkali and silica (Figs. 12a–12g). Electron microprobe analysis found little evidence for pervasive phyllosilicate or ferric oxide alteration, but rather distinct alteration textures and relatively similar compositions for the primary minerals (feldspars, pyroxene, olivine, and opaques).

VSWIR spectra weathering trends

Overall shape varies from relatively flat (relatively pristine basalt with minor coatings and phyllosilicates; J) to downward sloping (presence of coatings and small amounts of phyllosilicates; B) to concave down (clay-like; C and A) as alteration increases. This suggests an overall trend from relatively pristine basalt to thin coatings to well-ordered phyllosilicates. The band depth at 0.53 μm (BD530) and the slope between 0.6 and 0.8 μm increase with increasing alteration (as determined

by changes in continuum shape, petrographic textures, and chemistry of discrete mineral phases). This suggests an overall trend in increasing ferric iron and oxidation as alteration progresses. BD1900 increases with increasing sample alteration based on visual analysis (amount of red material on surface) and overall continuum shape. BD1900 also correlates with both BD530 and BD2210 suggesting a continuous alteration trend of increasing hydration (BD1900), iron oxidation (BD530), and Si/Al-OH bearing phases (BD2210; Figs. 4a, 4b, and 4c). A similar overall trend is reflected in the correlation between BD2210 and BD530, suggesting a trend of increasing Si/Al-OH bonds and oxidation as alteration progresses (Figs. 4d and 4e). Band depths at longer wavelengths (BD2210 and BD2290) show little correlation, indicating that Fe/Mg-OH and Si/Al-OH for well-crystalline hydrated silicates are not strongly related (Fig. 4a). BD2290 and BD530 are also not correlated, possibly indicating iron oxide formation is not closely related to the processes that create Fe-OH and Mg-OH bearing phases in these samples.

Bulk-chemistry weathering trends

The bulk-rock samples all plot in the basanite field and have little variation in bulk composition (Fig. 1; Table 2). The chemical index of alteration (CIA) values for all samples range from 0.526 (sample A) to 0.505 (sample J). On a classic diagram used in studies of terrestrial and martian weathering (e.g., Nesbitt and Wilson 1992; Nesbitt and Young 1989), there is little evidence for mobility of cations and chemical alteration. Despite the similarity in bulk composition, some trends between silica and other
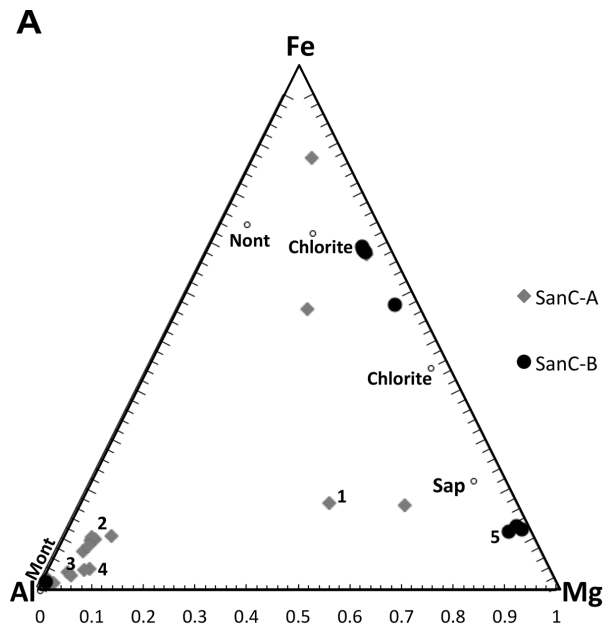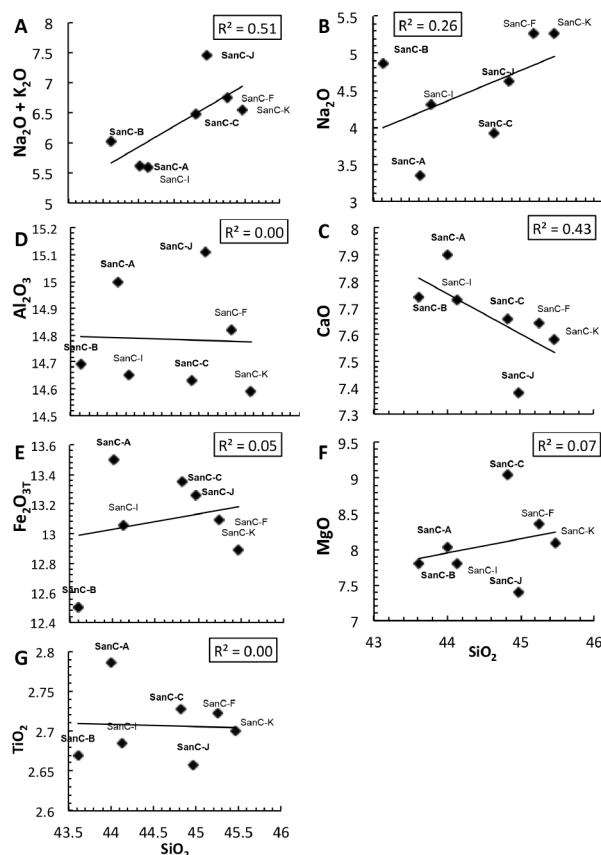

◄**FIGURE 10. (a)** Composition of potential clay minerals (in mol%) calculated on the basis of 11 oxygen atoms, as determined by electron microprobe analyses; most clay-like minerals in SanC-A plot near montmorillonite (Mont), consistent with spectral data. Clay-like compositions in SanC-B plot along the Fe-Mg axis, indicating the presence of more Fe,Mg-rich phyllosilicates. The single SanC-B analysis near the Al-vertex was taken from altered material between plagioclase laths; most phyllosilicate-like compositions for B were found near altered olivine grains, and few phyllosilicates were found near plagioclase laths. No clays were found with microprobe in SanC-J or SanC-C. Labeled points on ternary are shown in BSE images for **(b)** SanC-A and **(c)** SanC-B.
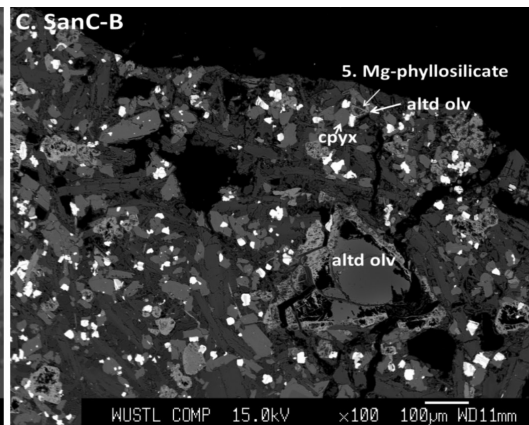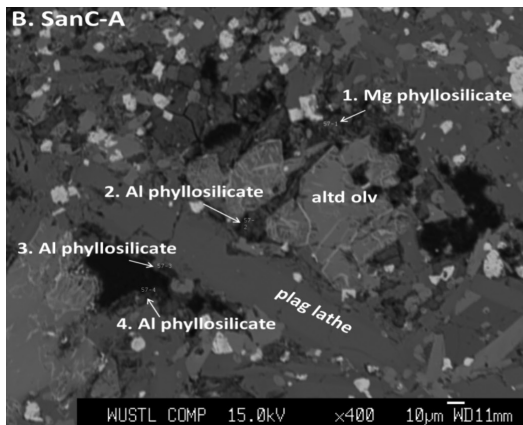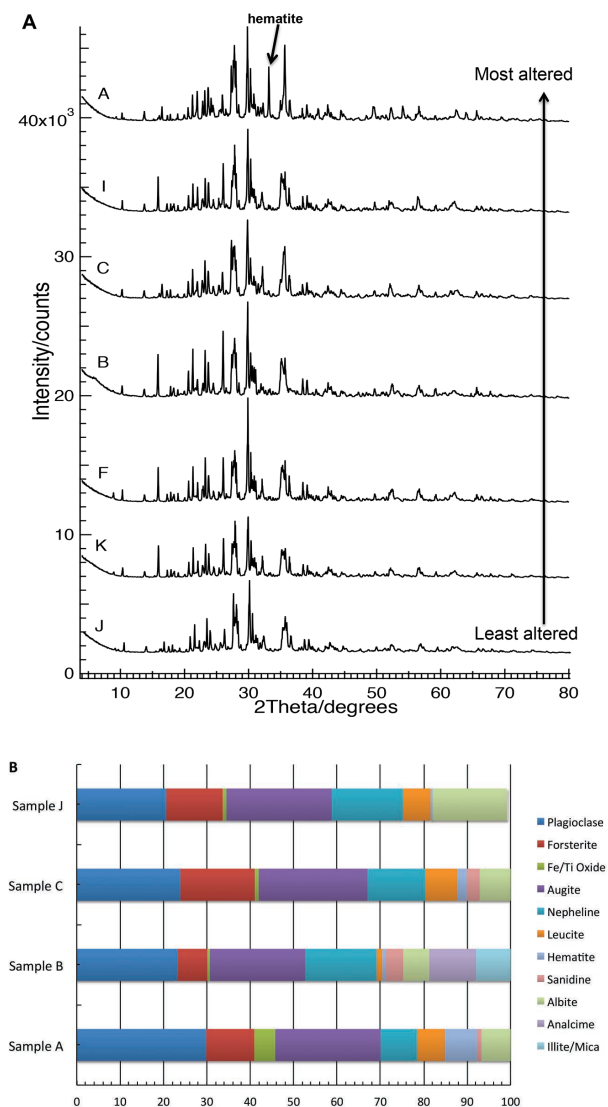
FIGURE 11. (**a**) XRD spectra offset along the y-axis arranged from most altered (sample A) to least altered (sample J) showing sharp peaks from primary mineralogy, and broader features due to the presence of amorphous phases. The primary hematite peak is labeled in spectra A to show the change due to alteration from the sample J to A. (**b**) Calculated mineral abundances (in wt%) from XRD Rietveld analyses with end-member compositional information determined from microprobe analyses. (Color online.)

FIGURE 12. Bulk-chemical data in wt% vs. silica for all samples; samples selected for further study from spectra are shown in bold text, (**a**) alkalis vs. SiO_2, (**b**) Na_2O vs. SiO_2, (**c**) CaO vs. SiO_2, (**d**) Fe_2O_{3T} vs. SiO_2, (**e**) Al_2O_3 vs. SiO_2, (**f**) MgO vs. SiO_2, (**g**) TiO_2 vs. SiO_2. Trends are enrichment in Fe^{3+} and depletion of Si and Na due to alteration. The trend in Ca may be due to primary compositional variation and/or its relative enrichment as other elements are depleted (see **c**). Variation in Ti and Mg are due to differences in petrogenesis.

oxides or sums of oxides arise (Figs. 12a–12g). Silica and alkalis are positively correlated (Fig. 12a), with high-alkali, high-silica compositions corresponding to the less altered samples (J, K, and F) and lower-alkali, lower-silica compositions corresponding to more highly altered samples (B, A, and I). A similar correlation occurs for silica and Na_2O (Fig. 12b). CaO and silica are negatively correlated (Fig. 12c); higher silica (less altered) samples are lower in CaO compared to lower silica (more altered) samples ($R^2 = 0.43$). This trend may be caused by preferential retention of CaO during weathering or by Ca-rich fluids. The former seems favored by the lack of evidence for salts in most samples (except the surface of F) and the pristine pyroxene grains observed in

altered rocks. Al_2O_3 and Fe_2O_{3T} are not correlated with Si (Figs. 12d and 12e). MgO remains relatively constant for all values of silica (Fig. 12f). In general, for common basaltic minerals and glass, glass is the first to weather, followed by olivine, pyroxene, and then plagioclase (Eggleton et al. 1987). The typical ion mobility relationship is Na > K > Ca > Si > Mg > Al > Ti > Fe for basaltic weathering (Gislasson et al. 1996). Na and K are assumed to be mainly released from the weathering of plagioclase. Na_2O and K_2O contents typically decrease with increasing alteration, and this trend is found for these samples (Fig. 12a). Mg and Ca, released by weathering of olivine and pyroxene, respectively, typically decrease with increasing alteration, but that is not the case for these samples. Both elements are retained, along with Fe, while Si does appear to have been transported in a similar manner to the alkalis. Plots of oxides vs. loss on ignition (LOI) show interesting trends relating to changes in chemistry with hydration and/or oxidation (Figs. 13a–13c). LOI is strongly inversely correlated with silica content (Fig. 13a); lower LOI values correspond to higher silica values (less-altered samples; $R^2 = 0.76$). A similar inverse correlation occurs between LOI and

alkali content (Fig. 13b), suggesting that more altered samples (A, B, and I) have higher LOI values and lower alkali content compared to less altered samples ($R^2 = 0.58$). CaO and LOI are positively correlated (Fig. 13c), with more altered samples having high LOI and high CaO compared to less altered samples ($R^2 = 0.61$). In these samples, we infer that the most mobile cations were (in order of decreasing mobility) Na, K, Si, Fe, Mg, Ca, and Al. The lack of weathering of pyroxene appears essential for these trends.

Comparison of oxides to spectral parameters shows similar trends as oxide-oxide plots. BD1900 negatively correlates with alkali content, suggesting a relationship between increasing hydrous alteration and decreasing alkali content due to cation mobility (Figs. 14a–14d). However, BD1900 is not correlated with Fe_2O_{3T} ($R^2 = 0.03$). Some more altered (higher BD1900) samples are preferentially enriched in Fe_2O_{3T}, potentially due to the formation of Fe^{3+} oxides observed in Samples A, B, and C. Sample C is anomalous in that it has relatively high Fe_2O_{3T}, but BD1900 is low compared to all samples (Fig. 14d). Similar trends found in silica and BD1900 plots are seen in comparisons of BD530 with alkalis (Fig. 15a). Alkali content generally decreases with increasing BD530; this trend is controlled by the strong negative correlation between BD530 and Na_2O, due to the mobility of Na in basaltic weathering pathways. BD530 shows a strong positive correlation with Fe_2O_{3T}, and band depth increases with increasing Fe_2O_{3T} content (Fig. 15c). Both BD1900 and BD530 show a positive correlation with CaO, possibly due to the lack of weathering of Ca-rich pyroxenes (Figs. 14b and 15d).

Electron microprobe mineralogical analyses of alteration

On the basis of point analyses and traverses of individual grains, alteration processes were found to affect individual minerals differently, adding context to the general weathering patterns given by VSWIR spectra and bulk chemistry. Most minerals identified by VSWIR spectra were verified by microprobe data; hematite, Al smectite, Fe/Mg phyllosilicates, olivine, and high-Ca pyroxene were all identified through BSE imaging and spot analyses.

For olivine grains, edges were altered to "veiny" textures composed of hematite or another Fe^{3+} oxide like goethite or ferrihydrite. Highly altered olivine grains were transformed into a "mesh" of hematite [or other Fe^{3+} oxide] veins, with only small areas of Fe^{2+}-rich olivine remaining. Primary olivine grains are unzoned in the least altered sample (J), and olivine phenocrysts in altered samples (A, B, and C) have magnesian cores. Olivine grains in altered samples have rims that are higher in Fe owing to primary compositional zoning or oxidation to hematite; hematite alteration is indicated by a vermicular texture on the olivine grain rim. Analyses show both compositional zoning (Fe-rich rims vs. Mg-rich cores) and mixing of olivine with altered hematite veins (Fig. 6). There is no silica directly (spatially) related with this alteration, thus it appears that silica was mobile and lost from the grain, as was Mg, thought these elements were not always clearly lost from the bulk sample. Two traverses across larger olivine grains in J and C also found olivine-pyroxene intergrowths. Pyroxene was found to vary little; most compositions plot in the augite field (average composition of $Wo_{39}En_{48}Fs_{13}$) and alteration textures similar to those for olivine were not observed, indicating
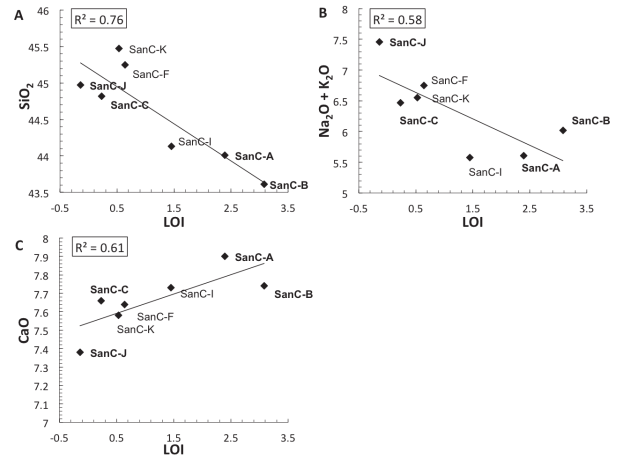
FIGURE 13. Loss on ignition (LOI) vs. various oxides in wt% (**a**) SiO_2, (**b**) alkalis, and (**c**) CaO track alteration with depletion in alkalis and silica, and slight enrichment in Ca with increasing LOI, which is interpreted to represent hydration of the sample upon alteration.
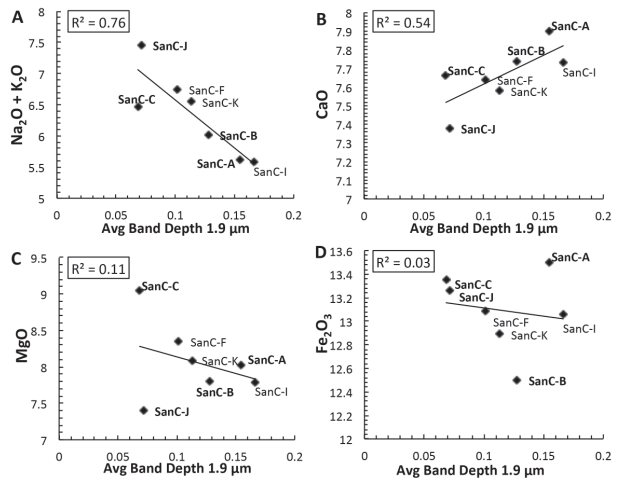
FIGURE 14. Weight percent oxides vs. band depth at 1.9 μm (BD1900; tracks H_2O) for all samples; bold types indicate sample subset used for further analyses. (**a**) General weathering trend of depletion in alkalis with increasing alteration (water content) due to weathering of plagioclase, (**b**) slight trend in CaO with water content perhaps caused by persistence of plagioclase and Ca-rich pyroxene as samples are weathered; no evidence of Ca-salt precipitation was observed within the rock though exterior surfaces of Sample F had acquired precipitated gypsum. (**c**) MgO, and (**d**) Fe_2O_{3T} shows no consistent trends with BD1900, possibly because of different alteration styles observed in particular samples.

this phase was not susceptible to alteration (as also observed by Eggleton et al. 1987).

Typical feldspar compositions for samples J, A, and C fall within a plagioclase composition (between An_{30} and An_{70}). Analyses in sample B found alkali-rich rims (average composition $An_2Ab_{46}Or_{52}$) along the edges of plagioclase laths reflecting overgrowth of plagioclase grains by material precipitated from evolved residual melt (Fig. 9). Mottled textures were found for many feldspar laths in A, B, and C, and alkali-rich feldspars

(average compositions $An_5Ab_{47}Or_{48}$ and $An_5Ab_{75}Or_{20}$) were detected on lath edges in sample C (Fig. 5). More pristine feldspar samples have higher anorthite components, and overall higher amounts of Ca, while more altered samples have more alkali-rich compositions. All samples contain dark, unaltered phases between plagioclase laths, consistent with nepheline compositions. Smaller laths of leucite are also present in A and C.

Opaque phases were found as discrete grains of titanomagnetite and intergrowths of both titanomagnetite and ulvöspinel. This latter occurrence may be the result of exsolution of ulvöspinel as samples are altered (Price 1980). Alternatively, the ulvöspinel and titanomagnetite intergrowth could be a primary texture from cooling or changes in oxygen fugacity of the original lava. For example, ulvöspinel and titanomagnetite exist as one phase at high temperatures; as temperature decreases, ulvöspinel exsolves out as a separate phase. Textures of the zoning are irregular and amoeboid-like for the most altered sample (A), and angular/well-defined for less altered samples (B and C). No zoning was observed in the least altered sample (J), all opaques were titanomagnetite. In addition to zoning, titanomagnetite altered to ilmenohematite, indicating increased oxidation (Fig. 8). Phyllosilicate alteration was not pervasive, and most measurements of potential clay minerals were limited to a few micrometers distance from the edges of the plagioclase laths or altered olivine. Highly altered phases with frayed edges in the interstices between feldspar laths, around olivine edges, and in vesicles are likely poorly ordered phyllosilicates. Weight percent totals for most of the inferred phyllosilicates were low, between 80 and 90%, consistent with 10 to 20% water contents, typical for many smectites. Ternary diagrams of Al, Fe, and Mg, common cations in smectite octahedral sites, show most phyllosilicate-like materials in sample A plotting near the Al vertex, near montmorillonite. Phyllosilicate-like compositions in sample B fall between Mg and Fe, suggesting trioctahedral smectites (Fig. 10).

Possible alteration pathways

Overall alteration trends, as opposed to distinct weathering pathways, are suggested by bulk-chemical data and comparison of oxides with spectral parameters (Figs. 16 and 17a). Comparisons of BD1900 and BD2210 suggest an alteration pathway from J to C and A, characterized by a change from amorphous silica to Al-smectites with greater hydration of feldspars and accompanying formation of Fe-oxides from olivine, ulvospinel, and titanomagnetite. Comparison of BD2210 and BD530 suggests an overall alteration trend related to increasing amorphous silica and/or well-ordered Al-phyllosilicates, as well as oxidation.

BD2290 shows no correlation with BD1900 ($R^2 = 0.0054$) when considering all samples, however, sample B has a large BD2290 value compared to all other samples. This indicates that sample B might represent the early stages of alteration, where only the most susceptible mineral, olivine, is dissolved to form Fe/Mg-phyllosilicates. Alteration may not have been pervasive enough in sample B to also form Al-phyllosilicates, like those present in samples A and C. Thus, sample B, compared to samples A and C, might be a less weathered example of the same alteration pathway that formed samples A and C. Alternatively, sample B might represent an alternate weathering regime where Fe from dissolved olivine is preferentially incorporated
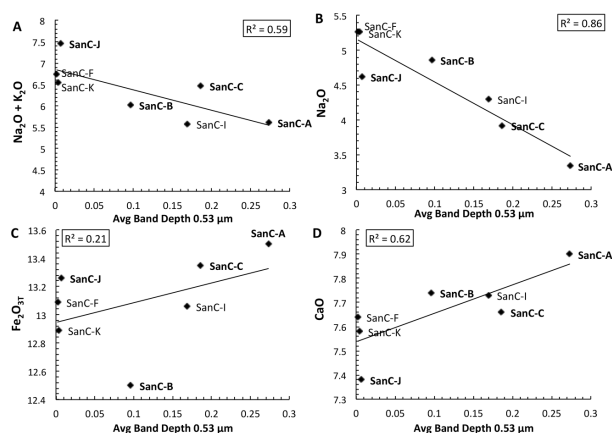

FIGURE 15. Weight percent oxide vs. band depth at 0.53 μm (BD530; tracks Fe^{3+}-oxides) for (**a**) alkalis vs. BD530, which shows a trend in depletion of alkalis (controlled by Na) with increasig BD530, (**b**) Na_2O vs. BD530, which shows the trend in alkali depletion is dominated by loss of Na, (**c**) Fe_2O_{3T} vs. BD530 shows increasing oxidation ferric iron content, and (**d**) CaO vs. BD530 shows a small enrichment in Ca. SanC-B is an outlier (as in Fig. 14d) for iron.

into phyllosilicates, and Fe is not oxidized to form hematite or other Fe^{3+} oxides (Fig. 12d).

The trend of decreasing alkalis with decreasing silica in feldspars emphasizes the direct relationship in bulk-chemical compositions and suggests something about cation mobility as these samples are altered. It is possible that decreasing alkali content in the bulk composition is related to the weathering of plagioclase grains as alteration progresses (Fig. 17b). Increasing Ca with increasing silica content in the bulk composition may be caused by retention of Ca due to the lack of pyroxene alteration, as other primary phases are weathered. LOI (as a measure of sample hydration) is negatively correlated with alkali and SiO_2 content and confirms the trend of increasing hydration (as measured by B1900) with decreasing alkali and SiO_2, related to the loss of alkalis due to the weathering of feldspars as alteration progresses.

Data from the electron microprobe indicates increasing oxidation, loss of alkalis (Na and K), and the formation of Al-OH and/or Fe/Mg-OH phyllosilicates as samples are altered (Fig. 17c). The wormy intergrowths of titanomagnetite and ulvöspinel in the most altered sample (A) contain ilmenohematite from the oxidation of titanomagnetite. Further evidence for persistent iron oxidation is indicated by Fe^{3+} oxide rims or a "mesh" of Fe^{3+} oxide veins in olivine grains for altered samples (A, B, and C). Fe^{2+}, concentrated in the rims of zoned olivine grains, is oxidized to Fe^{3+} as alteration progresses. Olivine grain rims, then, are preferentially altered to poorly crystalline hematite [or other Fe^{3+} oxide], as evidenced by the veiny "mats" of poorly crystalline Fe^{3+} oxide on olivine rims in B and A. As alteration progresses, the Fe-rich rims of olivine grains are completely altered to a pseudo-hematite phase and orange-colored veins pervade through the Mg-rich olivine core. Mottled plagioclase laths in altered samples indicate some alteration of plagioclase, which may relate to decreasing alkali content trends seen in the bulk-chemical data. Frayed grains along the edges of plagioclase
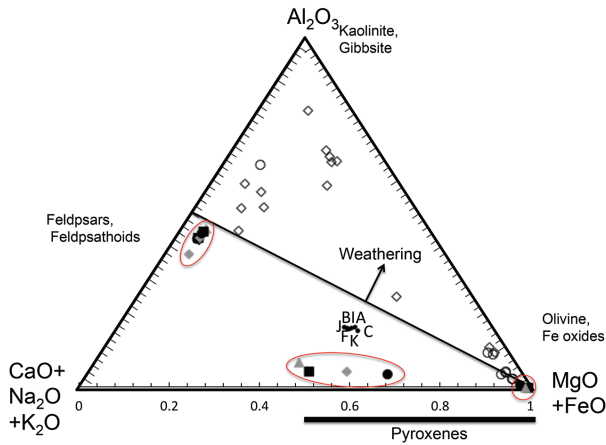
FIGURE 16. Ternary diagram of Al, Ca/Na/K, and Fe/Mg for bulk compositions (in mol%) of all samples (labeled with sample letters); red circles show the fields for feldpsars/feldspathoids, pyroxenes, and olivine. The arrow shows the general open-system weathering trend for basalts after Nesbitt and Wilson (1992). Closed symbols represent primary minerals, while open symbols show altered minerals. (Color online.)

laths may represent phyllosilicates formed from plagioclase alteration (Fig. 10). Weathering of plagioclase releases alkalis (Na and K), Ca, Al, and Si. Most of the alkalis are lost, resulting in the general trend of decreasing alkali content relative to Si; however, it is possible that some K is incorporated with Al into leucite ($KAlSi_2O_6$), as leucite is only present in altered samples A, B, and C. Al and Si are retained, and likely incorporated into phyllosilicates along the edges of mottled plagioclase laths, resulting in the relative immobility of Al compared to Si seen in bulk-chemical data. Compositions for these grains plot near the Al vertex of the Al-Fe-Mg diagram, verifying the Al-rich phyllosilicate signatures seen in VSWIR spectra for two of the altered samples (A and C). Si and Mg are lost as the more Mg-rich olivine is dissolved, and incorporated into the Fe/Mg phyllosilicates found along the edges of altered olivine grains in B. Analyses for frayed grains along the edge of altered olivine grains plot along the Mg-Fe join, verifying spectral data of saponite or other Fe/Mg phyllosilicates. Thus, Al clays are likely created by the alteration of plagioclase laths, while Fe/Mg phyllosilicates are formed from altered Mg-rich olivine (as also seen by Velde and Nicot 1985). The Fe-rich rims of the zoned olivine are oxidized to form pervasive pseudo-hematite veins, and titanomagnetite is also oxidized to form ilmenohematite, causing ulvöspinel to exsolve out as a secondary phase. Pyroxene and nepheline, both present in unaltered sample, J, and persistent in all altered samples, remain pristine and show no signs of alteration (Fig. 17d).

IMPLICATIONS

In the context of recent discoveries on Mars by MER and MSL, it is evident that alkaline basaltic rocks are present on Mars, and their primary mineralogy, as well as any alteration products, needs to be further studied (McSween et al. 2006; Stolper et al. 2013). The San Carlos suite of high-alkali basalts (basanites), studied here, with moderately high-alkali percentages and feldspathoid phases is particularly relevant as an analog.
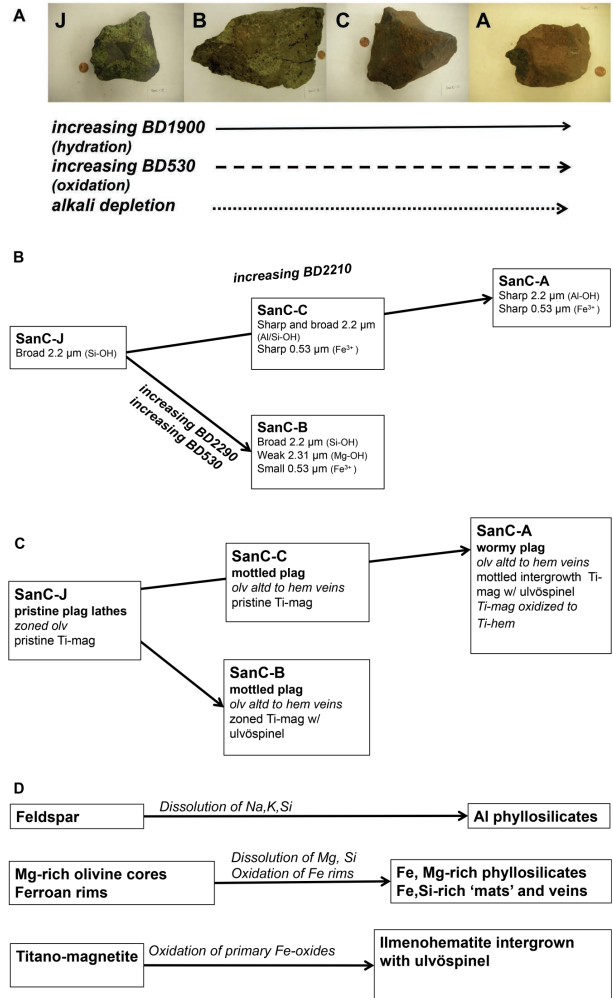
FIGURE 17. Overall weathering trends from (**a**) spectral and bulk-chemical data, (**b**) spectral data at longer wavelengths, (**c**) secondary textures and point analyses from the microprobe, and (**d**) primary and secondary mineralogy. Arrows indicate the direction from least to most altered. (Color online.)

VSWIR spectral analyses detected metal-OH absorptions and Fe^{3+} electronic transitions of secondary minerals formed by hydrous alteration and oxidation. Signs of hydration and oxidation are also seen in bulk-chemical data in the San Carlos suite as trends of various oxides vs. LOI or silica; however, both bulk chemistry and electron microprobe analyses show that samples have undergone mainly isochemical alteration, with only subtle compositional variations accompanying alteration in Na, K, and Si (Fig. 16). XRD analyses provide identification and structural information on the primary phases within samples. They are sometimes sensitive to the presence of clays and other amorphous substances, but did not identify the small amounts of clays observed here with the other techniques. Electron microprobe microanalysis reveals the effects of oxidation and also that the development of clay minerals is subtle. BSE images of alteration textures showed altered mineral phases indicated by VSWIR data, and spot analyses also revealed the effects and extent of

oxidation. Areas around the edges of wormy plagioclase laths and oxidized olivine grains were found to contain phyllosilicate-like compositions, corresponding to the phyllosilicate identifications from the spectral data. Evidence for the oxidation of iron (Fe^{2+} to Fe^{3+}) is also evident in analyses of mottled titanomagnetite and ulvöspinel intergrowths in the most altered sample (A). Alteration was most prevalent within a few millimeters of the sample's surface. The samples still contain mostly primary mineralogy with some incipient alteration.

The nature of alteration observed here over the last 2–3 Ma for the San Carlos alkaline basalts is similar to results from some studies of subalkaline basalts. Salvatore et al. (2013) found limited formation of crystalline products in oxidative weathering rinds of basalts from Antarctica, and Ehlmann et al. (2012) found evidence for mostly closed-system alteration in basalts in contact with Icelandic groundwater systems. In contrast, Greenberger et al. (2012) found mostly open system weathering in Deccan traps basalts. The main controls on alteration style and secondary mineralogy appear to be time, temperature, and the activity of H_2O. In this way, San Carlos is intermediate in alteration extent between the Antarctica samples analyzed by Salvatore and the Icelandic samples analyzed by Ehlmann. San Carlos samples show less evidence for well-crystalline alteration products, but have similar spectral signatures to the Icelandic samples analyzed by Ehlmann. The presence of additional alkalis does not appear to appreciably change the secondary mineralogy. As expected from prior work (e.g., Nesbitt and Wilson 1992), the alkalis are most readily mobilized. They are one of the few elements with measurable chemical trends here. Aiuppa et al. (2000) inferred the dissolution susceptibility of primary minerals to be olivine > clinopyroxene > plagioclase in alkaline basalts altered by CO_2-rich groundwater, although here we found olivine > plagioclase > pyroxenes.

Formation of Fe^{3+}-bearing oxides, silica, and/or Al/Fe/Mg phyllosilicates is similar to mineral assemblages observed on Mars at multiple locations. Al smectites, Fe/Mg smectites, Fe oxides, and hydrated silica have been identified in multiple locations (e.g., Ehlmann and Edwards 2014). Nearly isochemical alteration during oxidation and hydration, as observed in San Carlos samples, seems to be typical of several formations on Mars showing evidence of alteration (e.g., Ming et al. 2008; Ehlmann et al. 2011; McLennan et al. 2014) albeit with several notable exceptions for particular rock formations where leaching is more extensive (e.g., Clark et al. 2007b; Arvidson et al. 2014; Hurowitz et al. 2016). There are some differences between the primary chemistry and mineralogy of our samples vs. martian ones. For example, our samples have less magnesium and iron than some martian alkaline basalts, and nepheline and leucite have not yet been identified on Mars. Perhaps most significantly, the altered San Carlos rocks have fewer amorphous phases than reported by CheMin for all rock and sand samples at Gale crater so far (e.g., Treiman et al. 2014; Bish et al. 2014). If the amorphous phase(s) are secondary products of alteration (rather than primary volcanic or impact glass), this may be a result of the faster reaction kinetics at warmer San Carlos, Arizona, facilitating the formation of Fe oxides and phyllosilicates. Yet, these Fe oxides and phyllosilicates products in the San Carlos rocks were apparently undetectable with XRD, instead being revealed by a combination of VSWIR spectroscopy and electron microprobe chemical analyses. This is likely because they are not yet well crystalline on the scales being probed by X-rays, and they are relatively low in abundance. One possibility is that martian sedimentary rocks at Gale crater are actually more altered (bulk percent alteration products) but to alteration products equally or less well-crystalline than those in our San Carlos rocks. Further sampling of materials at the Gale crater site and investigations with future, different payload suites are required to investigate this hypothesis.

The use of various techniques elucidates the sensitivity of each method to alteration products (clays and Fe oxides), primary mineralogy, and alteration styles/extent. VSWIR's sensitivity to hydrated silicates is apparent in this study, where the most altered sample showed sharp, deep absorptions beyond 2.2 μm, indicating the presence of silica and/or montmorillonite, even in relatively "pristine" samples. Analysis with the electron microprobe suggests that alteration was most pervasive on the outer surface, but evidence of weathering and dissolution was visibly apparent throughout the sample. For the XRD data, primary minerals (plagioclase, alkali feldspars, nepheline, augite, and titanomagnetite) were easily detected and the relative abundances matched those determined from visual analysis in petrographic microscopes and backscattered electron microprobe images. Secondary minerals, such as phyllosilicates and ferric oxides, were identified in all samples in the spectra, but low abundances meant precise amounts were difficult to determine with microprobe or XRD. Combined with VSWIR data from orbit or ChemCam analyses from the first few micrometers of a sample, XRD provides primary mineralogy and detection of well-crystalline alteration minerals and abundant amorphous phases. VSWIR's sensitivity to alteration products, including the ability to identify iron oxides and the major cation in phyllosilicates, even when poorly crystalline, is a useful complement to primary mineralogy abundances determined from more intensive geochemical methods.

Thus this study demonstrates that the existence of evidence of aqueous alteration, its extent/style, and weathering pathways can be better understood using multiple techniques. Bulk geochemistry was useful, in this work, for determining that alteration was mainly isochemical and that cation exchanges occurred in a closed system, with the exception of alkali and silica loss. This finding has important implications for alpha particle X-ray spectroscopy (APXS) on MER, as bulk-chemistry plots provide insight on the mobility of cations compared to typically immobile cations, and aid in understanding alteration styles. The presence of iron oxides is an important indicator of alteration style and oxidation extent, and the MER instruments had this capability with Mössbauer spectrometers, although MSL does not. For the Mars-2020 rover mission with SuperCam (Raman, LIBS, VSWIR), scanning habitable environments with Raman and luminescence for organics and chemicals (SHERLOC), planetary instrument for X-ray lithochemistry (PIXL), combined spectroscopy and geochemistry techniques will be critical (Maurice et al. 2015; Allwood et al. 2015; Beegle et al. 2014). PIXL and SHERLOC will not be able to replace the capabilities of microprobe spot analyses of individual grains, but for sand-sized and larger grains, it might be possible to determine differences in weathering

textures and primary and secondary mineral assemblages even within phases. The detection of phyllosilicates and ferric iron may be challenging, depending on specific instrument sensitivities at the sub-pixel level. SuperCam SWIR spectroscopy (1.3 to 2.6 um) combined with SuperCam passive VNIR spectroscopy and Mastcam-Z (0.4–1.0 um) multispectral imaging will be crucial for recognizing slightly aqueously altered rock outcrops and mapping subtle trends, as demonstrated here.

Given the identification of primary mineralogy and alkaline composition in many rocks at Gale crater by MSL, the San Carlos suite constitutes a useful terrestrial analog in terms of both primary and secondary alteration mineralogy. The use, in this work, of combined spectroscopy and geochemistry methods serves as a proof of concept for the importance of complementary methods in both current and future missions. The implications of this work have special relevance for Mars2020, and will motivate the use of instruments on MER and MSL to better understand aqueous alteration on Mars.

ACKNOWLEDGMENTS

REFERENCES CITED

Aiuppa, A., Allard, P., D'Alessandro, W., Michel, A., Parello, F., Treuil, M., and Valenza, M. (2000) Mobility and fluxes of major, minor and trace metals during basalt weathering and groundwater transport at Mt. Etna volcano (Sicily). Geochimica et Cosmochimica Acta, 64, 1827–1841.

Allwood, A. et al. (2015) Texture-specific elemental analysis of rocks and soils with PIXL: The Planetary Instrument for X-ray Lithochemistry on Mars 2020. Aerospace Conference 2015 IEEE, 1–13.

Armstrong, J.T. (1995) CITZAF-a package of correction programs for the quantitative electron microbeam X-ray analysis of thick polished materials, thin films, and particles. Microbeam Analysis, 4, 177–200.

Arvidson, R.E. et al. (2014) Ancient aqueous environments at Endeavour crater, Mars. Science, 343, 1248097.

Beegle, L.W. et al. (2014) SHERLOC: Scanning habitable environments with raman and luminescence for organics and chemicals, an investigation for 2020. AGU Fall Meeting Abstracts, 1, 6.

Bibring, J.P. et al. (2006) Global mineralogical and aqueous Mars history derived from OMEGA/Mars Express data. Science, 312(5772), 400–404.

Bish, D. et al. (2014) The first X-ray diffraction measurements on Mars. IUCrJ, 1, 514–522.

Bishop, J.L., Pieters, C.M., and Edwards, J.O. (1994) Infrared spectroscopic analyses on the nature of water in montmorillonite. Clays and Clay Minerals, 42, 702–714.

Bishop, J.L., Lane, M.D., Dyar, M.D., and Brown, A.J. (2008) Reflectance and emission spectroscopy study of four groups of phyllosilicates: Smectites, kaolinite-serpentines, chlorites, and micas. Clay Minerals, 43, 35–54.

Blaney, D.L., Wiens, R.C., Maurice, S., Clegg, S.M., Anderson, R.B., Kah, L.C., and Madsen, M.B. (2014) Chemistry and texture of the rocks at Rocknest, Gale Crater: Evidence for sedimentary origin and diagenetic alteration. Journal of Geophysical Research: Planets, 119, 2109–2131.

Clark, R.N., King, T.V.V., Klejwa, M., and Swayze, G.A. (1990) High spectral resolution reflectance spectroscopy of minerals. Journal of Geophysical Research, 95(B8), 12,653–12,680.

Clark, R.N., Swayze, G.A., Wise, R., Livo, E., Hoefen, T., Kokaly, R., and Sutley, S.J. (2007a) USGS digital spectral library splib06a. U.S. Geological Survey, Digital Data Series 231, http://speclab.cr.usgs.gov/spectral.lib06.

Clark, B.C. et al. (2007b) Evidence for montmorillonite or its compositional equivalent in Columbia Hills, Mars. Journal of Geophysical Research: Planets, 112(E6), doi:10.1029/2006je002756.

Clegg, S.M., Wiens, R.C., Barefield, J.E., Sklute, E., and Dyar, M.D. (2009) Quantitative remote laser induced breakdown spectroscopy by multivariate analysis. Spectrochimica Acta Part B, 64, 79–88.

Clegg, S.M., Anderson, R.B., Forni, O., Lasue, J., Dyar, M.D., Morris, R.V.,

Ehlmann, B.L., McLennan, S.M., Bender, S., Cousin, A., and others. (2014) Expansion of the ChemCam calibration database. Lunar Planetary Science XLV, 2378.

Clegg, S.M., Wiens, R.C., Anderson, R.B., Forni, O., Frydenvang, J., Lasue, J., Pilleri, A., Payre, V., Boucher, T., Dyar, M.D., and others. (2016) Recalibration of the Mars Science Laboratory ChemCam instrument with an expanded geochemical database. Spectrochimica Acta Part B, in press.

Cousin, A. et al (2015) Igneous rock classification at Gale (Sols 13–800). Lunar Planetary Science Conference, Abstract 2452.

Eggleton, R.A., Foudoulis, C., and Varkevisser, D. (1987) Weathering of basalt: Changes in rock chemistry and mineralogy. Clays and Clay Minerals, 35.3, 161–169.

Ehlmann, B.L., and Edwards, C.S. (2014) Mineralogy of the martian surface. Annual Reviews of Earth and Planetary Science, 42, 291–315.

Ehlmann, B.L., et al. (2011) Subsurface water and clay mineral formation during the early history of Mars. Nature, 479, 53–60.

Ehlmann, B.L., Bish, D.L., Ruff, S., and Mustard, J.F. (2012) Mineralogy and chemistry of altered Iceland basalts: Application to clay mineral detection and understanding aqueous environments on Mars. Journal of Geophysical Research, 117(E11).

Ehlmann, B.L., et al. (2013) An expanded training set for processing MSL Chem-Cam LIBS data: Spectral library samples added and effects on elemental compositional results from Mars. Lunar and Planetary Science XXXXIV.

Farrand, W.H., Bell, J.F. III, Johnson, J.R., Squyres, S.W., Soderblom, J., and Ming, D.W. (2006) Spectral variability among rocks in visible and near-infrared multispectral Pancam data collected at Gusev crater: Examinations using spectral mixture analysis and related techniques. Journal of Geophysical Research, 111, EO2S15.

Frey, F.A., and Prinz, M. (1978) Ultramafic inclusions from San Carlos, Arizona: Petrologic and geochemical data bearing on their petrogenesis. Earth and Planetary Science Letters, 38, 129–176.

Gellert, R., et al. (2013) Initial MSL APXS activities and observations at Gale Crater, Mars. Lunar and Planetary Science XXXXIV.

Gislasson, S.R., Arnorsson, S., and Armannsson, S. (1996) Chemical weathering of basalt in Southwest Iceland: Effects of runoff, age of rocks, and vegetation/ glacial cover. American Journal of Science, 296, 837–907.

Golden, D.C., Ming, D.W., Morris, R.V., and Mertzman, S.A. (2005) Laboratory-simulated acid-sulfate weathering of basaltic materials: Implications for formation of sulfates at Meridiani Planum and Gusev Crater, Mars. Journal of Geophysical Research, 110, E12S07.

Greenberger, R.N., Mustard, J.F., Kumar, P.S., Dyar, M.D., Breves, E.A., and Sklute, E.C. (2012) Low temperature aqueous alteration of basalt: Mineral assemblages of Deccan basalts and implications for Mars. Journal of Geophysical Research, 117, E00J12.

Grotzinger, J.P., Crisp, J., and Vasavada, A.R. (2015) Curiosity's Mission of Exploration at Gale Crater, Mars. Elements, 11, 19–26.

Hausrath, E.M., Navarre-Sitchler, A.K., Sak, P.B., Steefel, C.I., and Brantley, S.L. (2008) Basalt weathering rates on Earth and the duration of liquid water on the plains of Gusev crater, Mars. Geology, 36, 67–70.

Hurowitz, J.A., and McLennan, S.M. (2007) A ~3.5 Ga record of water-limited, acidic weathering conditions on Mars. Earth and Planetary Science Letters, 260, 432–443.

Hurowitz, J.A., McLennan, S.M., Lindsley, D.H., and Schoonen, M.A.A. (2005) Experimental epithermal alteration of synthetic Los Angeles meteorite: Implications for the origin of martian soils and identification of hydrothermal sites on Mars. Journal of Geophysical Research, 110, E07002.

Hurowitz, J.A., et al. (2016) Dynamic geochemical conditions recorded by lakebed mudstones in Gale Crater, Mars. Lunar and Planetary Science XXXXVII.

Maurice, S. et al. (2012) The ChemCam instruments on the Mars Science Laboratory (MSL) rover: Science objectives and mast unit. Space Science Reviews, 170 95–166.

Maurice, S. et al. (2015) The SuperCam Instrument for the Mars2020 Rover. European Planetary Science Congress, 10, 185.

McLennan, S.M. et al. (2014) Elemental geochemistry of sedimentary rocks at Yellowknife Bay, Gale Crater, Mars. Science, 343(6169), 1244734.

McSween, H.Y. et al. (2006) Alkaline volcanic rocks from the Columbia Hills, Gusev crater, Mars. Journal of Geophysical Research, 111, E09S91.

Meslin, P.-Y. et al. (2013) Soil diversity and hydration as observed by ChemCam at Gale Crater, Mars. Science, 341, doi:10.1126/science.1238670.

Milliken, R.E., and Mustard, J.F. (2005) Quantifying absolute water content of minerals using near-infrared reflectance spectroscopy. Journal of Geophysical Research, 110, E12001.

Ming, D.W. et al. (2008) Geochemical properties of rocks and soils in Gusev crater, Mars: Results of the Alpha Particle X-ray Spectrometer from Cumberland Ridge to Home Plate. Journal of Geophysical Research: Planets, 113(E12), doi:10.1029/2008je003195.

Minitti, M.E., Weitz, C.M., Lane, M.D., and Bishop, J.L. (2007) Morphology, chemistry, and spectral properties of Hawaiian rock coatings and implications for Mars. Journal of Geophysical Research: Planets, 112(E5), doi:10.1029/2006je002839.

Morris, R. et al. (2000) Mineralogy, composition, and alteration of Mars Pathfinder rocks and soils: Evidence from multispectral, elemental, and magnetic data on terrestrial analogue, SNC meteorites, and Pathfinder samples. Journal of Geophysical Research, 105(E1), 1757–1817.

Mustard, J.F., et al. (2005) Olivine and pyroxene diversity in the crust of Mars. Science, 307, 1594–1597.

Mustard, J.F., Murchie, S.L., Pelkey, S.M., Ehlmann, B.L., Milliken, R.E., Grant, J.A., Bibring, J.P., Poulet, F., Bishop, J., Dobrea, E.N., and others. (2008) Hydrated silicate minerals on Mars observed by the Mars Reconnaissance Orbiter CRISM instrument. Nature, 454, 305–309.

Nesbitt, H.W., and Wilson, R.E. (1992) Recent chemical weathering of basalts. American Journal of Science, 292, 740–777.

Nesbitt, H.W., and Young, G.M. (1989) Formation and diagenesis of weathering profiles. The Journal of Geology, 97, 129–147.

Pelkey, S.M., et al. (2007) CRISM multispectral summary products: Parameterizing mineral diversity on Mars from reflectance. Journal of Geophysical Research: Planets, 112(E8), doi:10.1029/2006je002831.

Price, G.D. (1980) Exsolution microstructures in titanomagnetites and their magnetic significance. Physics of the Earth and Planetary Interiors, 23, 2–12.

Rogers, A.D., and Christensen, P.R. (2007) Surface mineralogy of martian low-albedo regions from MGS-TES data: Implications for upper crustal evolution and surface alteration. Journal of Geophysical Research, 112, E01003.

Salvatore, M.R. et al. (2013) Development of alteration rinds by oxidative weathering processes in Beacon Valley, Antarctica, and implications for Mars. Geochimica et Cosmochimica Acta, 115 137–161.

Sautter, V. et al. (2014) Igneous mineralogy at Bradbury Rise: The first ChemCam campaign at Gale crater. Journal of Geophysical Research: Planets, 119, doi:10.1002/2013je004472.

Sautter, V. et al. (2015) In situ evidence for continental crust on early Mars. Nature Geoscience, 8, 605–609.

Schmidt, M.E. et al. (2014) Geochemical diversity in first rocks examined by the Curiosity Rover in Gale Crater: Evidence for and significance of an alkali and volatile-rich igneous source. Journal of Geophysical Research: Planets, 119, 64–81.

Skok, J.R., Mustard, J.F., Ehlmann, B.L., Milliken, R.E., and Murchie, S.L. (2010) Silica deposits in the Nili Patera caldera on the Syrtis Major volcanic complex on Mars. Nature Geoscience, 3, 838–841.

Stolper, E.M. et al. (2013) The petrochemistry of Jake_M: A martian mugearite. Science, 341, 1239463.

Sunshine, J.M., and Pieters, C.M. (1993) Estimating modal abundances from the spectra of natural and laboratory pyroxene mixtures using the Modified Gaussian Model. Journal of Geophysical Research, 98, E5, doi:10.1029/93je00677.

Treiman, A.H. et al. (2014) Ferrian saponite from the Santa Monica Mountains (California, USA, Earth): Characterization as an analog for clay minerals on Mars with application to Yellowknife Bay in Gale Crater. American Mineralogist, 99, 2234–2250.

Udry, A., Balta, J.B., and McSween, H.Y. (2014) Exploring fractionation models for martian magmas. Journal of Geophysical Research: Planets, 119, 1–18.

Vasavada, A.R., Grotzinger, J.P., Arvidson, R.E., Calef, F.J., Crisp, J.A., Gupta, S., and Yingst, R.A. (2014) Overview of the Mars Science Laboratory mission: Bradbury landing to Yellowknife Bay and beyond. Journal of Geophysical Research: Planets, 119, 1134–1161.

Velde, B., and Nicot, E. (1985) Diagenetic clay mineral compositions as a function of pressure, temperature, and chemical activity. Journal of Sedimentary Petrology, 55, 541–547.

Wiens, R.C. et al. (2012) The ChemCam instruments in the Mars Science Laboratory (MSL) Rover: Body unit and combined system performance. Space Science Reviews, 170, 167–227.

Wiens, R.C. et al. (2013) Pre-flight calibration and initial data processing for the ChemCam laser-induced breakdown spectroscopy instrument on the Mars Science Laboratory rover. Spectrochimica Acta Part B, 82, 1–27.